ABSTRACT

Methods are presented for calculating aerodynamic interference loads on aircraft components. The report treats wing-tail interference, effects of stores and effects of engines. In the first part, a simple method is proposed for calculating the load distribution on the tail in the presence of wing and fuselage. Next, a modified image method is described for calculating interference loads of wing-body-store combinations. The last part deals with the aerodynamic interference effects on lifting surfaces in the presence of either a propeller slipstream or a jet slipstream. General effects of small flow disturbances on aircraft loads are also considered briefly.

CONTENTS

SECTION		PAGE
I.	INTRODUCTION	1
II.	WING-BODY-TAIL INTERFERENCE	3
	A. INTRODUCTION	3
	B. DESCRIPTION OF THE METHOD	3
	C. NUMERICAL CALCULATION AND COMPARISON WITH EXPERIMENT	6
III.	INTERFERENCE EFFECTS ON ENGINE NACELLES AND STORES	9
	A. INTRODUCTION	9
	B. DESCRIPTION OF PROCEDURE	9
	1. General Remarks	9
	2. Calculation of Upwash Distribution on the Wing	11
	3. Stores and Engine Nacelles	14
	4. Effects of Wing Interference on Lift Distribution on Nacelle	17
	C. NUMERICAL CALCULATION AND EXPERIMENTAL DATA	19
IV.	SLIPSTREAM EFFECT	21
	A. INTRODUCTION	21
	B. FLOW FIELD GENERATED BY AN ISOLATED PROPELLER	21
	1. Propeller Operating at Zero Angle of Attack	21
	2. A Propeller Operating at an Angle of Attack α_T	24
	C. PROPELLER AND WING INTERACTIONS AT SUBSONIC SPEEDS	27
	D. "INTERFERENCE FLOW"	27
	1. Condition on the Trailing Vortex Sheet	29
	2. Conditions on the Boundary of the Slipstream	29

CONTENTS (Continued)

SECTION		PAGE
	E. COMPARISON WITH EXPERIMENT	32
	F. SIMPLIFICATION OF NUMERICAL CALCULATION	33
	G. JET SLIPSTREAM INTERFERENCE	33
	H. DISCUSSION ON NONUNIFORMITY	36
	APPENDIX	
	CALCULATION OF THE CHANGE IN CIRCULATION	37
	REFERENCES	43

ILLUSTRATIONS

FIGURE		PAGE
1.	Lift Distribution and Equivalent Vortex System	47
2.	Horseshoe Vortex System	48
3.	Coordinate System	48
4.	Airplane Configuration	49
5.	Comparison of Calculated Lift on Wing-Body Combination with Experiment	50
6.	Comparison of Calculated Lift on Wing-Body-Tail Combination with Experiment	51
7a.	Missile Configuration	52
7b.	Comparison of Theoretical and Experimental Normal Force Coefficient on Tail in Presence of Wing and Body	52
8.	The Spanwise Loading on the Modified Wing	53
9.	The Trailing Vortex System of the Wing-Body-Nacelle Combination	54
10.	Image Vortex System Due to Right Wing Vortices	55
11.	Downwash Calculation	55
12.	Image Vortex Inside a Nacelle	56
13.	The Corresponding Vortex System of the Propeller Slipstream	57
14.	The Coordinate System and the Wing's Corresponding Vortex Sheet	57
15.	Experimental and Calculated Values of ΔC_l (after Ferrari[4])	58
16.	Experimental and Calculated Values of ΔC_D (after Ferrari[4])	59
17.	Jet Wake with Turbulent Mixing Profile for a Typical Jet Engine (Static Sea Level Case)	60

SYMBOLS

a	perturbation parameter defined by Eq. (25)
a	geometrical parameter defined by Eq. (13)
a_1	radius of the cross-section of the body
a_2, a_3	radius of the cross-section of the nacelle
A	parameter defined by Eq. (39a)
$A_{\nu\nu}$	quantities defined in Appendix Eq. (A-7)
$A_{\nu\eta}$	quantities defined in Appendix Eq. (A-7)
AR	aspect ratio
b	wing total span
b	geometrical parameter defined by Eq. (13)
$b_{\nu\nu}$, $b_{\nu\eta}$	Multhopp coefficients defined in Eq. (A-7) of Appendix
B	parameter defined by Eq. (39b)
$B_{\nu\nu}$, $B_{\nu\eta}$	quantities defined in Appendix Eq. (A-7)
c	wing chord
$c(y)$	local chord
c	geometrical parameter defined by Eq. (13)
c_ℓ	section lift coefficient
C_L	total lift coefficient
C_D	drag coefficient
C_T	defined by the thrust relation $T = 4C_T R_1^2 \rho_\infty U_\infty^2$ where R is the radius of the actuator disk
C_p	pressure coefficient

SYMBOLS (Continued)

C_m	pitching moment coefficient
C_g	defined by the equation $Z + \alpha_T T = (C_g + \alpha_T C_T) 4R^2 \rho_\infty U_\infty^2$ where Z is the body force in z-direction
ℓ/d	the fineness ration of the body
E	the complete elliptic integral of the second kind
F	force
f_w	semi-span of the wing tip vortex
g_w	one-half the distance between the wing image vortices in the body
H	sink strength
$I_{\mu\nu}, J_{\mu\nu}$	quantities defined by Eq. (A-7)' in Appendix
K	source strength
K	the complete elliptic integral of the first kind
L	lift
ℓ	the streamwise distance between the midchord on the tail and the point where the wing root chord and the line of center of pressure of the wing intersect
ℓ	body length
m	number of spanwise stations on the wing
m'	quantities defined by Eq. (39)
M_∞	free stream Mach number
M_ν, M_ν'	quantities defined by Eq. (A-7) in Appendix
n', n''	quantities defined by Eq. (39)
N_ν, N_ν'	quantities defined in Appendix Eq. (A-7)
p	pressure

SYMBOLS (Continued)

q	dynamic pressure = $\frac{1}{2}\rho U_\infty^2$
r	circular body radius
r_i	distance between the vortex and the point
R	radius of the slipstream
R_1	radius of the actuator disk
s	local semi-span, including body
S	velocity ratio parameter defined by $S = \frac{V_2}{V_1} = 1 + 2aB^2$
T	thrust
U_∞	free stream velocity
u	x axis-component of velocity perturbation
v	y axis-component of velocity perturbation
V	velocity
v_x, v_y, v_z	velocity increments in x, y, and z-axis directions respectively
w	z axis-component of velocity perturbation
w	upwash velocity
w_f	upwash due to the angles of attack of body and nacelle
$w_t(\alpha_t)$	downwash due to the tail geometrical angle of attack in the uniform flow
w	induced downwash due to the wing interference
w_B	body induced upwash
w_{td}	downwash due to the circulation changes introduced by the disturbance in the oncoming flow arriving at the tail
w_{Bd}	body change in upwash introduced by the disturbed flow
w_a, w_b, w_{ab}	upwash velocities defined by Eqs. (19), (20), (21)

SYMBOLS (Continued)

x	streamwise coordinate
$x_{c.p.}$	streamwise center of pressure location
y	spanwise coordinate
z	vertical coordinate
Z	body force in z direction
α	angle of attack
α_B	local body angle of attack
α_w	local wing angle of attack
α_t	local tail angle of attack, also angle of attack of the propeller disk
α_t'	effective tail angle of attack defined by Eq. (16)
β	$\sqrt{1-M^2}$
$\mathcal{B}$	quantities defined in the Appendix
$\gamma(y)$	nondimensional form of the circulation defined on page 30
$\gamma_p(\theta)R\,d\theta$	the strength of the bound vortices in any sector of the circular system of vortices where $d\theta$ denotes the angular amplitude of the sector in question
γ	specific heat ratio
Γ	vortex strength
Γ_m	defined by the Eq. $\Gamma_m = \frac{1}{\rho_\infty U_\infty}\left(\frac{dL}{dy}\right)_m$ where $\left(\frac{dL}{dy}\right)_m$ is the maximum of the loading curve
η	spanwise coordinate
θ_i	angle defined by Sketch 5
ξ	streamwise coordinate

SYMBOLS (Concluded)

Π	the complete elliptical integral of the third kind
ρ	density
ρ_∞	free stream density
σ	tail sweepback angle (at the midchord)
σ_w	wing sweepback angle (at the center of pressure line)
ϕ	velocity potential
Φ	angle defined by $\tan^{-1}\frac{U_\infty}{\omega R}$
Ψ	stream function, also represents potential in slipstream flow case
$(\,)_\infty$	free stream properties or quantities
$(\,)_I$	properties or quantities outside the slipstream
$(\,)_{II}$	properties or quantities inside the slipstream

SECTION I

INTRODUCTION

Aerodynamic interference effects have become of more concern in recent years because of the increasing utilization of high speed low aspect ratio wing and slender body combinations. Available procedures for calculating aerodynamic load distributions for structural design purposes are evaluated in Ref. 1. Some modifications and extensions of these methods may be found in Ref. 2 and Ref. 3 . The present report describes methods for estimating aerodynamic loads due to wing-tail interference, external store effects and engine slipstream effects. The physical models, on which calculations of interference effects are based, are assumed to apply from low subsonic to moderate supersonic speeds ($M \sim 4$). In each speed range, however, the appropriate aerodynamic theories must be used to obtain the flow fields and loads.

To calculate effects of wing-tail interference, an equivalent horseshoe vortex system is used to replace the flow field around a lifting wing-body combination. Experimental results show that the trailing vortex sheets tend to roll up after a short distance behind the lifting surface and to form two concentrated tip vortices. The boundary condition at the body surface requires the addition of two corresponding image vortices in the body. The flow at the tail is determined by superimposing the downwash due to the vortex system on the local angle of attack. Now the tail-body combination can be treated as a wing-body problem with the modified angle of attack distribution. Circulation changes on the tail due to the disturbance of the nonuniform flow are also discussed. The proposed procedure for calculating loads gives generally good agreement with experiment but it may be inaccurate in certain unfavorable geometric situations.

Interference loads on the wing due to the presence of nacelles may be calculated by a modified Gray and Schenk method. Upwash induced by the nacelle is calculated by slender body theory. The numerical program developed in Ref. 2 may be modified for application to the calculation of the interference load distribution.

Methods for calculating propeller slipstream interference effects are described in Refs. 4 to 8. A general description of the method is presented in this report. Some extensions and modifications of the method are made in order to calculate the jet slipstream effects on lifting surfaces. The Appendix provides a procedure to treat small disturbance nonuniform flow within the limit of linear theory.

SECTION II

WING-BODY-TAIL INTERFERENCE

A. INTRODUCTION

Once the aerodynamic loads on a wing-body combination are calculated the circulation distribution at the trailing edge of the wing may be estimated, and an equivalent horseshoe vortex system may also be constructed. The trailing vortex sheets are assumed to be fully rolled up after a short distance behind the wing and to form two tip vortices plus two corresponding image vortices in the body. A downwash distribution due to this vortex system may be calculated at the tail. The angle of the flow deflection from the main stream due to the downwash is superimposed on the local tail angle of attack. The tail-body combination with this modified angle of attack distribution may now be treated as a wing-body problem in calculating the aerodynamic loads.

B. DESCRIPTION OF THE METHOD

After the lift on a wing has been calculated the circulation distribution at the wing trailing edge may be found immediately from the relation $\Gamma = (dL/dy)/\rho_\infty U_\infty$. A typical lift (and vortex strength) distribution is shown by the solid curve in Fig. 1.

Trailing vorticity has a tendency to roll up on itself as explained in Ref. 9. The measurements reported in Ref. 10 indicate that after about one chord length behind the wing trailing edge, the trailing vorticity may be represented by a single tip vortex on each side of the fuselage. The strength of the concentrated vortex will be $\Gamma_m = \frac{1}{\rho_\infty U_\infty}\left(\frac{dL}{dy}\right)_m$ where $\left(\frac{dL}{dy}\right)_m$ is the maximum of the loading curve. The vortex position is determined by the condition, indicated by the dotted rectangle in Fig. 1, that the total lift on the configuration must be equal to the vortex strength times the span between vortices. Hence

$$f_w - g_w = \frac{L}{2\rho_\infty U_\infty \Gamma_m} \tag{1}$$

where L is the lift on the wing-body combination. The position of the image vortex is determined by the boundary condition on the body surface which requires

$$r_w^2 = f_w g_w \tag{2}$$

This result is, of course, only valid for circular bodies. The more general elliptic case is described in Part I of this report (Ref. 2).

The lift on the wing may also be represented by a single concentrated bound vortex. Finally a horseshoe vortex system is formed which now represents the total disturbance caused by the presence of the wing and forebody (see Fig. 2).

The downwash on the tail due to the horseshoe vortices must next be calculated. In the computations, the downwash at the tail is assumed to be constant over the chord of the tail and equal to the value at the mid-chord. All the calculations are based on the selected mid-chord line on the tail.

Let (x, y, z) be a control point on the mid-chord of the tail and

ℓ = the streamwise distance between the mid-chord on the tail and the point where the wing root chord and the line of center of pressure of the wing intersect.

σ_t = tail sweepback angle (at the mid-chord).

σ_w = wing sweepback angle (at the center of pressure line).

Also let r_i be the distance between ith vortex and the point (x, y, z). Then from the geometry (see Fig. 3) we have the following relations.

$$r_1 = \left[(f_w - y)^2 + h^2\right]^{1/2} \tag{3}$$

$$r_2 = \left[(y - g_w)^2 + h^2\right]^{1/2} \tag{4}$$

$$r_3 = \left[(y + g_w)^2 + h^2\right]^{1/2} \tag{5}$$

$$r_4 = \left[(y + f_w)^2 + h^2\right]^{1/2} \tag{6}$$

$$r_5 = \left[(\ell + y\tan\sigma_t - y\tan\sigma_w)^2 \cos^2\sigma_w + h^2\right]^{1/2} \tag{7}$$

$$r_6 = \left[(\ell + y\tan\sigma_t + g_w\tan\sigma_w + y\tan\sigma_w)^2 \cos\sigma_w + h^2\right]^{1/2} \tag{8}$$

and the corresponding downwash distributions are:

$$w_1 = \frac{\Gamma_m}{4\pi r_1^2}\left[1+\frac{l_1'}{(l_1'^2+r_1^2)^{1/2}}\right](z_w - y) \tag{9}$$

$$w_2 = \frac{\Gamma_m}{4\pi r_2^2}\left[1+\frac{l_2'}{(l_2'^2+r_2^2)^{1/2}}\right](y - g_w) \tag{10}$$

$$w_3 = \frac{+\Gamma_m}{4\pi r_3^2}\left[1+\frac{l_2'}{(l_2'^2+r_3^2)^{1/2}}\right](y + g_w) \tag{11}$$

$$w_4 = \frac{\Gamma_m}{4\pi r_4^2}\left[1+\frac{l_1'}{(l_1'^2+r_4^2)^{1/2}}\right](y + g_w) \tag{12}$$

where $l_1' = l + y\tan\sigma_t - (z_w - g_w)\tan\sigma_w$

$l_2' = l + y(\tan\sigma_t - \tan\sigma_w)$

and the downwash distributions due to the bound vortices are:

$$w_5 = \frac{\Gamma_m}{4\pi r_5^2}\left[\frac{a}{(r_5^2+a^2)^{1/2}} - \frac{b}{(r_5^2+b^2)^{1/2}}\right](l + y\tan\sigma_t - y\tan\sigma_w)\cos\sigma_w \tag{13}$$

$$w_6 = \frac{\Gamma_m}{4\pi r_6^2}\left[\frac{-c}{(r_6^2+c^2)^{1/2}} + \frac{(z_w\sec\sigma_w - g_w\sec\sigma_w + c)}{\left\{r_6^2+\left[(z_w - g_w)\sec\sigma_w + c\right]^2\right\}^{1/2}}\right] \cdot \tag{14}$$

$$\cdot (l + y\tan\sigma_t + g_w\tan\sigma_w + y\tan\sigma_w)\cos\sigma_w$$

where

$$a = \left[\ell_1'^2 + (f_w - y)^2 - \left\{ (\ell + y \tan \sigma_t - y \tan \sigma_w) \cos \sigma_w \right\}^2 \right]^{1/2}$$

$$b = (f_w - g_w) \sec \sigma_w - a$$

$$c = \left[\ell_2'^2 + (g_w + y)^2 - \left\{ \ell + y \tan \sigma_t + (g_w + y) \cos \sigma_w \right\}^2 \right]^{1/2}$$

Superimposing the downwash given by Eqs. (9), (10), (11), (12), (13) and (14), we have

$$w_f(x, y, 3) = w_1 + w_2 + w_3 + w_4 + w_5 + w_6 \qquad (15)$$

If the angle of attack of the tail has a distribution (without the wing present) of $\alpha_t = \alpha_t(x, y)$, then the modified angle of attack α_t' which includes the part of the wing-body-tail interference effects in the present approach is shown in the following equation.

$$\alpha_t' = \alpha_t(x, y) + \frac{w_f(x, y)}{U_\infty} \qquad (16)$$

Now, the tail-body combination is treated similar to the wing body interference problem (see Part I – Wing-Body Interference Effects) with this modified angle of attack. In each Mach number domain, the method chosen in Ref. (1) is used to calculate the total interference aerodynamic load on the tail.

The change of circulation on the tail due to the nonuniformity of the oncoming flow field is neglected here. However, if one feels the necessity to include this contribution the approximate method presented in the Appendix may be used.

It should also be noted that for a slender aircraft configuration the nonlinear contributions of load due to vortex separation, described in Part II – Nonlinear Effects, may also be incorporated in the procedures for calculating wing-body lift. More details are given in the following section, Numerical Calculation.

C. NUMERICAL CALCULATION AND COMPARISON WITH EXPERIMENT

In order to make use of the computer programs developed for calculating wing-body interference problems, subsonic lift distribution on a tail in the presence of a wing and body, and subsonic distribution on a body in the presence of a tail lifting surface are considered. However, some supersonic experimental results and simplified analogous analytical procedures may be found in Ref. 11.

The body may have an arbitrary distribution of elliptic cross-section and camber*. The horizontal (or nearly horizontal) portions of the tail are assumed to join the body. If analysis of configurations where the horizontal tail does not join the body, e.g. "T-tails" is required, some modifications then must be made.

For illustration the airplane shown in Fig. 4 is analyzed. Experimental results for this configuration may be found in Ref. 12. The load on the wing-body is first calculated by using the program of Ref. (2). Figure 5 shows that it agrees quite well with the experimental data. The wing-body-tail contribution may be determined by the method presented in Section B. The comparison with experimental data is shown in Fig. 6. It does not show as good agreement as the wing-body calculation. However, it may be seen that it gives some slight improvement over the load calculated simply by superimposing wing-body lift and tail-alone lift.

In the particular geometry examined here, the theory underestimates the wing downwash effect. Specifically the tapered wing will produce a trailing vortex sheet with considerable strength in the inboard region. This sheet evidently does not entirely roll up in the short distance to the tail and hence induces a larger downwash over the tail surface than would be predicted by the horseshoe vortex theory. However, for more slender type configurations with untapered wings the theory is in very good agreement with experiment. Figure 7 from Ref. 11 demonstrates this clearly.

The method presented in Section B does not include all possible effects; the total downwash on the tail surface should consist of five parts.

$$w_t(y,z) = w_t(\alpha_t) + w_i + w_B + w_{t_d} + w_{B_d}$$

where

$w_t(\alpha_t)$ is the downwash due to the tail geometrical angle of attack in the uniform flow.

w_i induced downwash due to the wing interference.

w_B body-induced upwash.

w_{t_d} downwash due to the circulation changes introduced by the disturbance in the oncoming flow arriving at the tail.

w_{B_d} change in body upwash introduced by the disturbed flow.

The magnitudes of the downwash w_{t_d} and w_{B_d}, assumed here to be negligible, depend on the geometrical configuration of lifting surfaces and bodies and relative location of components. The validity of

* If the body cross-section is not elliptical then it may be possible to approximate it by an ellipse whose axes correspond to the maximum dimensions.

the assumed vortex rolling up process is also dependent on these geometric considerations. If w_{4_d} and w_{2_d} were not neglected as shown in the previous case, a simple perturbation technique similar to one shown in the Appendix could be used for estimating their contributions.

SECTION III

INTERFERENCE EFFECTS ON ENGINE NACELLES AND STORES

A. INTRODUCTION

Effects of wing-body-nacelle interference are treated in the linear domain, i.e., the load distribution and flow field are calculated separately and all loads due to different causes are superimposed. Interference loads on the wing due to the presence of nacelles may be calculated by a modified Grey and Schenk method. Axisymmetric nacelles with variable contour are considered. Finally an approximate technique is introduced to calculate the unsymmetrical interference loads on nacelles due to the presence of wings.

B. DESCRIPTION OF PROCEDURE

1. General Remarks

Since a solution is lacking of the appropriate partial differential equation for the flow field which satisfies the boundary conditions of the rather complicated configuration of a wing-body-nacelle combination the same approximation is employed as in the calculation of the load distribution on a wing-body combination i.e., the load distribution flow fields and their interactions are first calculated for wing, body and nacelles separately.

First of all, the load distribution for the wing alone, or the so-called "exposed wing" is calculated, then the interference load caused by the flow around bodies (both fuselage and nacelles) in the presence of the wing is superimposed. Calculation of the forces on the body and nacelles would be divided into two parts, namely, the load on body and nacelles respectively and the interference loads. Iterating the process by using the revised load distribution to recompute the required flow fields might improve the results. However, in view of other approximations in the process, this refinement is not recommended.

The spanwise load distribution for the wing alone may be calculated by one of the methods of Section IVB, IVC, IVD or IVE of Ref. 1, depending on Mach number and aspect ratio.

The procedure for calculating the interference load on the wing due to the presence of body and nacelles is based on a modification of the method of Grey and Schenk (see Part I – Wing-Body Interference Effects). A model as shown in the sketch on the following page is chosen to demonstrate the details of the calculation. The wing-body junctions are shown as lying above the body mid-plane.

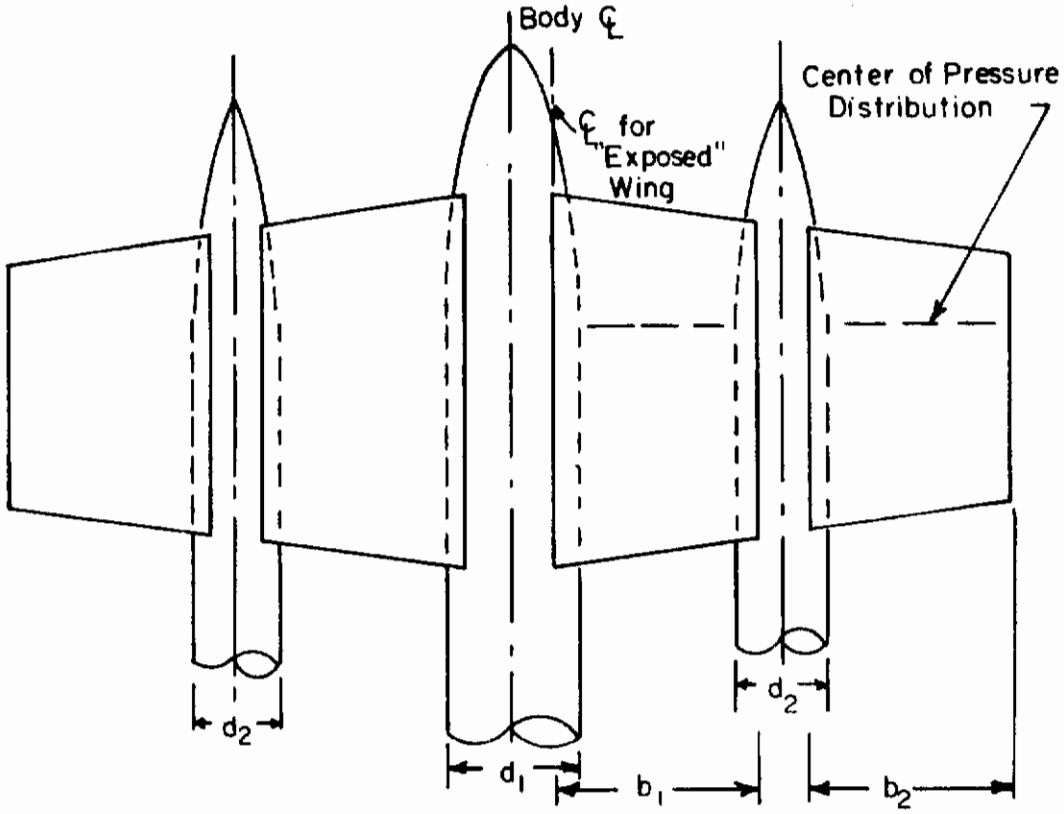

Sketch 1

Discontinuities at leading and trailing edges of the exposed wing may occur. However, in the present case, a modified exposed wing is used where straight lines are drawn from the wing tip to the wing root to replace those discontinuous edges. This is shown in Sketch 2.

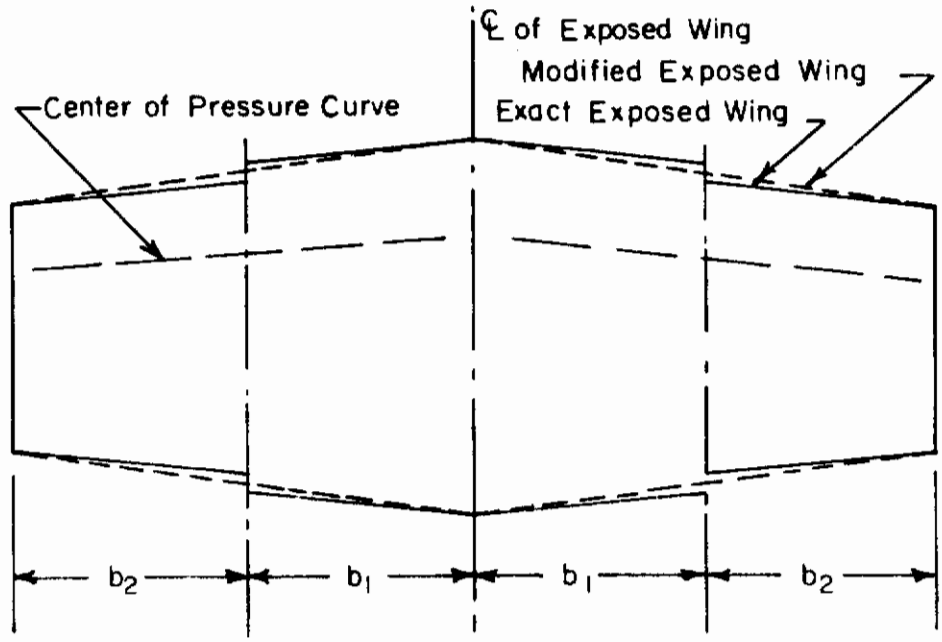

Sketch 2

The spanwise loading on that modified exposed wing along with the corresponding center of pressure distribution may be calculated by one of the methods stated previously. Results for a typical case are drawn in Fig. 8.

Interference loads on the wing may be calculated by steps similar to the ones described in Ref. 1.

a. Subdivide the spanwise load distribution on the modified exposed wing into a number of load increments. Discontinuities of the load distribution curve in Fig. 8 at locations of nacelles on the "real span" are neglected.

b. Replace increments by lifting horseshoe vortices.

c. Locate the image vortices within the body and nacelles.

d. Calculate the upwash distribution at control points due to these image vortices.

e. Add the upwash due to the body and nacelle angles of attack (if any).

f. Compute the wing load due to the total distribution of upwash at control points on the wing.

Details of these procedures are shown in the following section.

2. Calculation of Upwash Distribution on the Wing

In the first step, the spanwise loading is subdivided arbitrarily. The number of subdivisions must be sufficient to obtain a reasonable representation of the image vortex system. Consequently, the locations of nacelles on the wing influence the selection of the number of subdivisions. Sketch 3 gives a typical illustration.

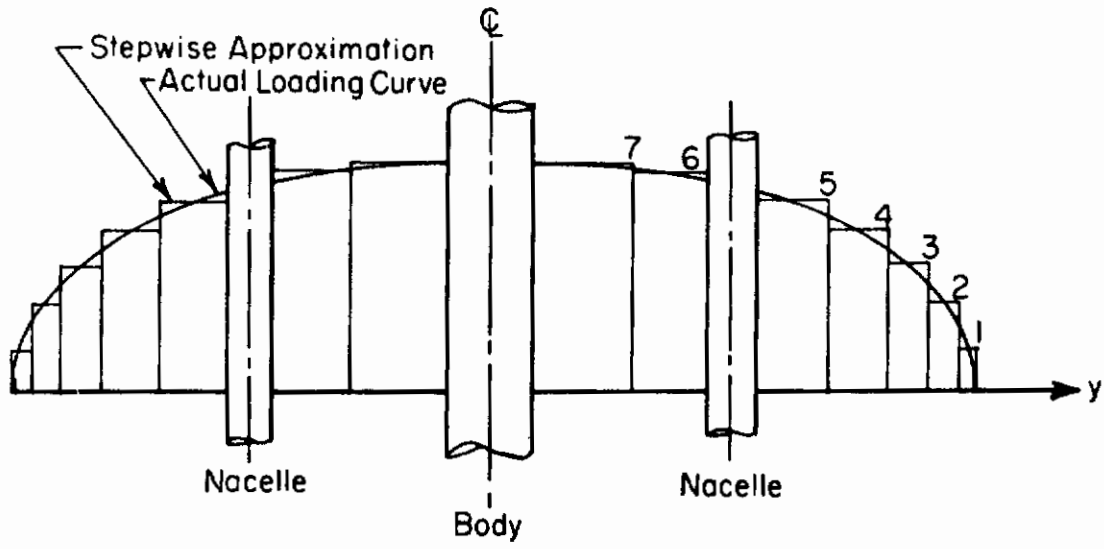

Sketch 3

Now each increment in spanwise loading may be replaced by a horseshoe vortex. The bound portion of the horseshoe is taken parallel to the spanwise coordinate and located approximately on the center of pressure line. The trailing portions extend to infinity in the streamwise direction. See Fig. 9.

Accordingly, the strength of vortex Γ_i' is proportional to the corresponding value of the stepwise approximation to the spanwise loading.

$$\Gamma_i' = \frac{1}{\rho_\infty U_\infty} \left(\frac{dL}{dy}\right) \tag{17}$$

where $(\,)_\infty$ corresponds to free stream properties. It is noted that an inboard trailing vortex lying adjacent either to the body or the nacelle is canceled by its image and is omitted from the computation.

The method of locating image vortices within the body has already been derived for circular cross-section bodies and for elliptical cross-section bodies[2]. Once again iteration of the imaging process is not recommended. The method of locating image vortices within the nacelles will now be described.

Circular cross-section nacelles are assumed here for demonstration. However, these procedures may be easily extended to the elliptical cross-section nacelles as in Ref. 2.

Let the circular cross-section have a radius of a. The image of a vortex at r_e is a vortex of equal strength but opposite sign located on a line joining the vortex to the center of the circular body. See sketch below.

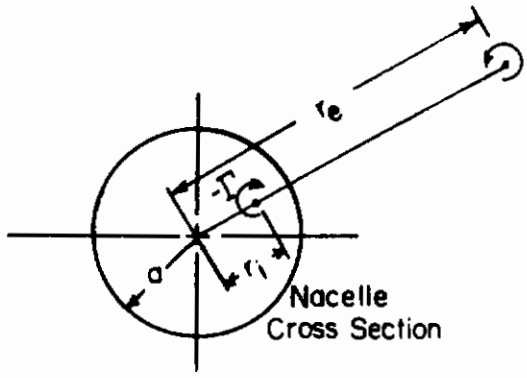

Sketch 4

The distance r_i' is given by $r_i' = \frac{a^2}{r_e}$ (18)

The image vortex is assumed to begin at the same axial station as the external wing vortex. The image of a complete horseshoe vortex is also assumed to consist of the images of the two trailing vortices whose starting points are joined by a straight vortex segment of the same strength approximating the image of the bound lifting vortex.

The wing is not symmetrical about the axis of the nacelle and the neighboring external vortices on both sides of the nacelle rotate in the same direction. Accordingly, all the image vortices within a nacelle rotate in the same direction but opposite to the external ones. This is the characteristic distinction between the wing-body combination and the wing-nacelle combination case. For example the image vortices corresponding to the trailing vortices behind the right half of the wing are shown in Fig. 10.

The location of a set of image vortices corresponding to any external horseshoe vortex may be found for bodies or nacelles of circular or elliptical cross-section.

A set of corrdinates is selected for each image horseshoe vortex as indicated in Fig. 11. The coordinates of the various vortices are related by the geometry of the wing-body-nacelle combination and may easily be determined.

Now a set of control points (x', y') is chosen along a line which is one half of the local chord behind the center of pressure at each spanwise station. The corresponding downwash at these points is obtained by addition of the following components.

$$w_a = w_{a(body)} + w_{a(nacelle)} = \sum_i \frac{\Gamma}{4\pi A_i^2}\left[1 + \frac{x_i'}{(x_i'^2 + A_i^2)^{1/2}}\right](y_i' + H_i \cos\gamma_i) \tag{19}$$

$$w_b = \sum_i \frac{-\Gamma}{4\pi B_i^2}\left[1 + \frac{x_i'}{(x_i'^2 + B_i^2)^{1/2}}\right](y_i' + H_i \cos\gamma_i) \tag{20}$$

$$w_{ab} = \sum_i \frac{-\Gamma}{4\pi}\frac{x_i \cos\gamma_i}{f_i^2 + x_i'^2}\left[\frac{(B_i^2 - f_i^2)^{1/2}}{(B_i^2 + x_i'^2)^{1/2}} - \frac{(A_i^2 - f_i^2)^{1/2}}{(A_i^2 + x_i^2)}\right] \tag{21}$$

where $'$ refers to the coordinate system for the i^{th} image vortex, and the quantities in these equations are defined by Fig. 11.

As stated before, the induced upwash due to the angle of attack of the body and the induced upwash due to the angles of attack of the nacelles are calculated separately in the original coordinate system, i.e., (x, y).

Let α_1 = angle of attack of the body (i.e., fuselage)
α_2, α_3 = angle of attack of a nacelle
R_1 = the distance between the axis of the body and the control station
R_2, R_3 = distance between the control station and the axis of a nacelle
a_1 = radius of the cross-section of the body
a_2, a_3 = radius of the cross-section of the nacelle
θ_i = angles defined in the following sketch

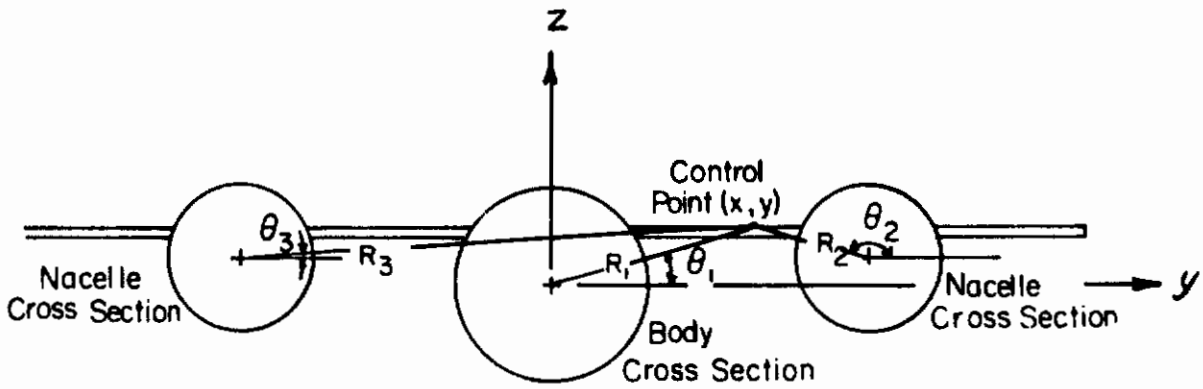

Sketch 5

Then, the upwash due to angles of attack of body and nacelles is

$$w_f = \sum_i V_\infty \alpha_i \frac{a_i}{R_i} \cos 2\theta_i \qquad (22)$$

Adding up the contributions of all image vortices from Eqs. (19), (20), (21) and (22) and dividing them by the free stream velocity, the local angles of attack are determined. The spanwise angle distribution due to this upwash is assumed to be uniform in the chordwise direction. Finally, the distribution of the interference wing load due to the presence of the body and nacelles may be obtained by applying one of the procedures stated in Section IVB, IVC, IVD, or IVE in Ref. 1 to this effectively twisted wing. Thus, the Weissinger method is chosen for high aspect ratio subsonic wings, to calculate the lift distribution, and the Lawrence method is used for low aspect ratio subsonic wing cases. Compressibility effect, as usual may be accounted for by the Prandtl-Glauert rule. In addition, Jones' theory seems capable of calculating the forces on transonic wings, and the linear supersonic theory is adequate for treating the supersonic cases. More details may be found in the references.

3. Stores and Engine Nacelles

The nacelles previously treated are semi-infinite axisymmetrical bodies with constant cross-section behind the nose. In the general case stores and nacelles not only have definite length, but also have variable contours. However, the corresponding image vortices at each section within the body with continuously varying circular or elliptical cross-sections may be found by the same method utilized in the previous section i.e., the constant cross-section case. Although it is still assumed that the strength of each image vortex is uniform it is no longer a straight line. See the sketch on the following page.

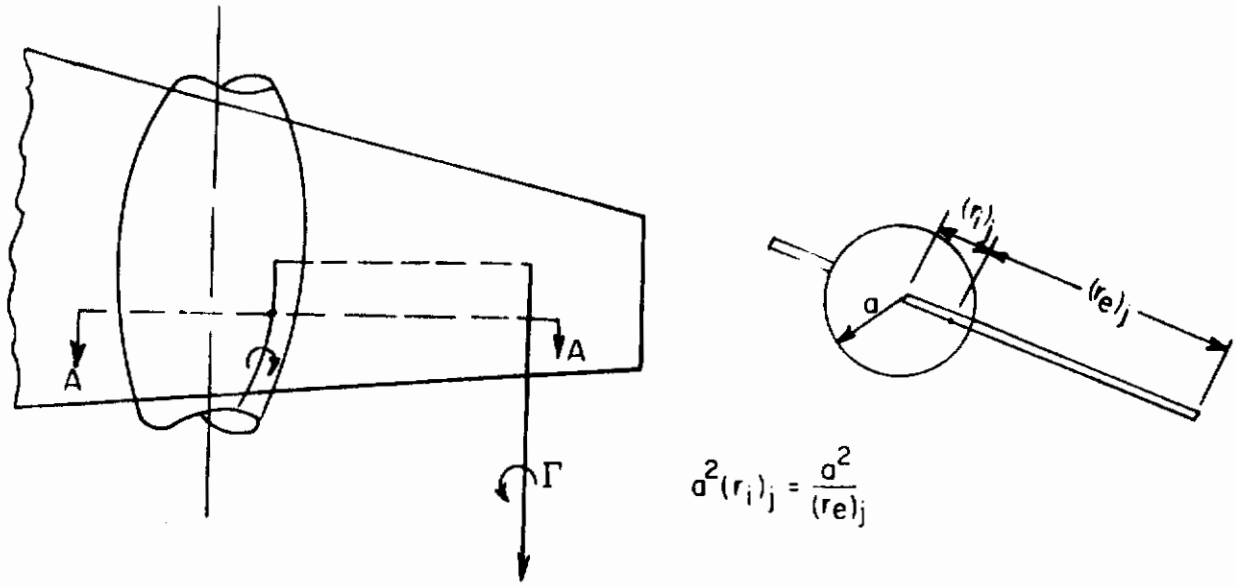

Sketch 6

For the sake of simplicity of the calculation the curved image vortex is replaced by an appropriate number of line segments. The induced downwash at the control station due to each vortex segment may be calculated by Eq. (24), given later in this section, once the geometric relations are determined.

For a sharp-nosed slender store the slender body theory may be used to calculate the upwash distribution on the wing induced by the store. The assumption is valid when $\beta/(\ell/d), \ll 1$ where $\beta = \sqrt{|1-M_\infty^2|}$ and (ℓ/d) is the fineness ratio of the body. A simple example of the flow about a cambered body of revolution taken from Ref.(13) will illustrate the procedure. The physical quantities are defined by the following sketch

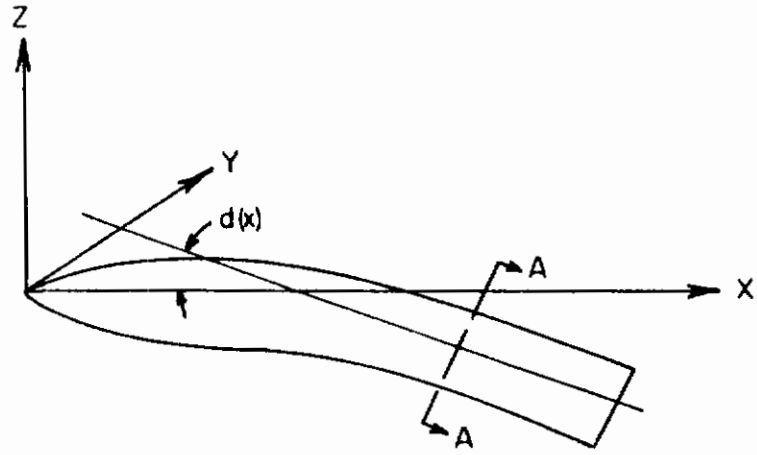

Sketch 7

Neglecting the small distortion of the shape of the cross-section due to the body camber. The flow pattern in the plane A-A appears as in Sketch 8.

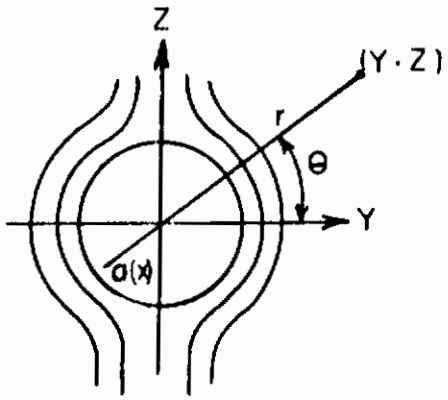

Sketch 8

The velocity potential is given by

$$\phi = U_\infty \sin\alpha(x)\, 3\left(1 + \frac{[a(x)]^2}{y^2+z^2}\right) + a\,\frac{da}{dx}\,U_\infty \ln\sqrt{y^2+z^2} \qquad (23)$$

where the second term accounts for the effects of the slope of the body contour. More details of the theory may be found in Refs. 1 and 13.

For the engine nacelle case, air flows through the nacelle and energy is transferred inside. The problem is sometimes more complicated. For instance, in the supersonic case the flow field may be as shown in the following sketch.

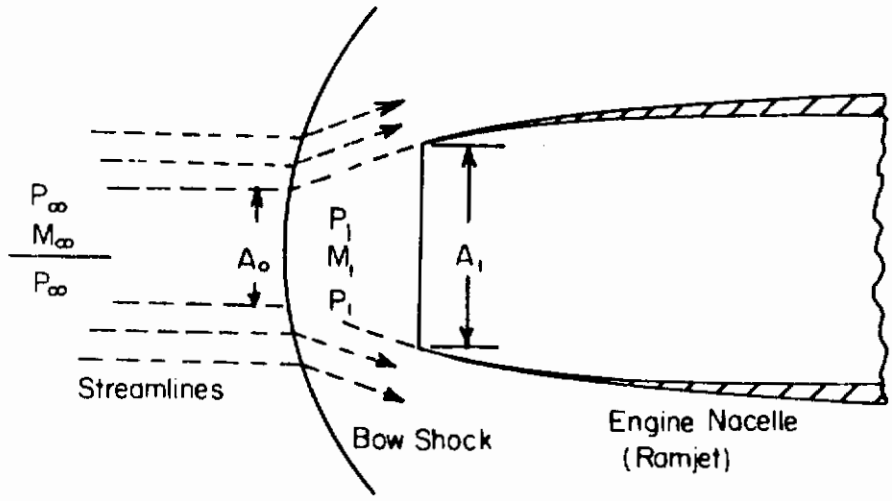

Sketch 9

Since the solution of the complete flow field around the nacelle is lacking, the following approximation is suggested for cases where the aerodynamic load on the wing due to nacelle interference is relatively small.

The inlet of the nacelle is extended to form a cone-like nose (see Fig. 12) and hence the problem becomes a search for the solution of the flow around a slender body, i.e., the slender body theory applies.

For example, the downwash due to the segment BC of the image vortex is

$$w_{BC} = \frac{\Gamma}{4h(f^2+h^2)}\left(\frac{\ell+\ell'}{c} - \frac{\ell'}{b}\right)\frac{b}{(f^2+h^2)^{1/2}} \qquad (24)$$

where projections of f, b, ℓ, ℓ', h, and c are defined in the same figure. Another approach to the flow around a body under a lifting wing may be found in Ref. 14.

4. Effects of Wing Interference on Lift Distribution on Nacelle

Since the nacelle structure must be designed to carry the weight of the engine, the interference load on nacelles is of secondary importance to the structural designer. Therefore, the following approximate calculation seems to be capable of giving reasonable results.

First, the interference load due to the presence of the wing and nacelle on the fuselage may be calculated by the method chosen in Section V of Ref. 1. However, it should be noted that during this part of the calculation the effect of nacelles on the body is neglected.

Secondly, the interference load on a nacelle due to presence of the wing alone (here the fuselage is ignored) may be calculated with a simplified model as shown in Sketch 10. This model will eliminate the troublesome unsymmetrical interference wing loads on nacelles. A rectangular wing shown by the dotted line in Sketch 10 is employed, and the problem is reduced to a simple wing-body interference calculation which may be treated by the method chosen in Ref. 1.

The dimensions of the wing are selected as follows; the span is chosen as twice the larger value of b_1 or b_2. The uniform chord of the wing is chosen equal to the wing chord on the axis of the nacelle. See Sketch 11.

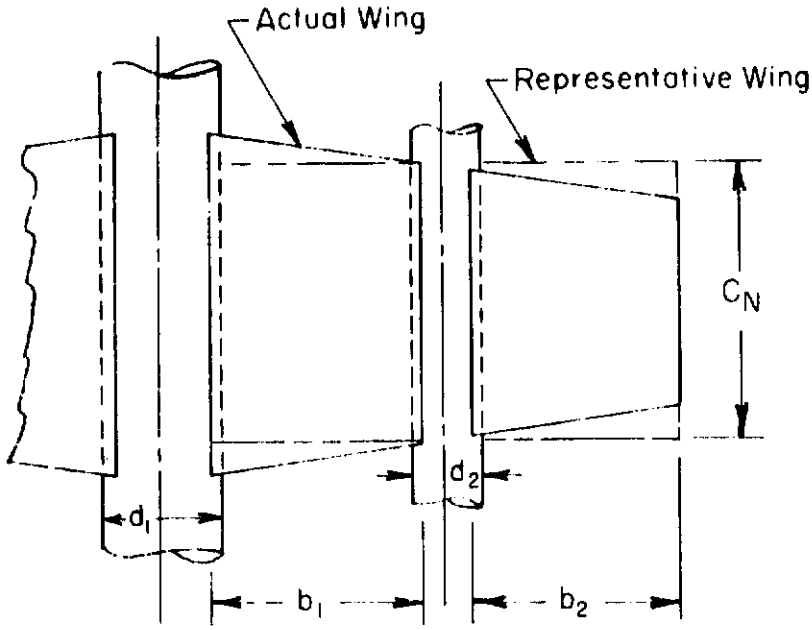

Sketch 10

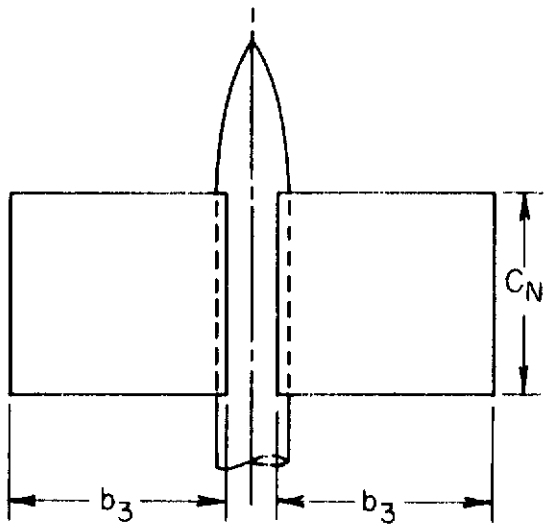

Sketch 11

C. NUMERICAL CALCULATION AND EXPERIMENTAL DATA

Numerical calculations may be carried out with the aid of computer programs developed for wing-body interference, but with extensive modification described in the previous Sections. Experimental data may be found in Refs. 15 to 23.

SECTION IV

SLIPSTREAM EFFECT

A. INTRODUCTION

A method for calculating the aerodynamic load distribution on lifting surfaces in the presence of propeller slipstream is described. In the calculation some simplified procedures are proposed. A method that is a modification of the previous one for calculating the jet slipstream effects is also included. Generally the present procedure may be used to calculate any small disturbance nonuniform flow around the lifting surface provided the linear assumption is valid.

The well-known actuator disk is used to represent the actual propeller. It is also assumed that the disk is placed sufficiently far away from the lifting surface that any variation in the velocity increments taking place along the axis of the slipstream may be neglected. The character of the slipstream which is induced by the propeller is assumed to be unchanged by the presence of the wing. The trailing vortex sheet behind the lifting surface is assumed to remain composed of straight-line vortices paralleled to the free stream. In other words, this vortex system is assumed to be uninfluenced by the induced velocities generated by the vortices shed from the propeller. In addition, the decay of the vorticity in the slipstream produced by viscosity and turbulence is not considered.

B. FLOW FIELD GENERATED BY AN ISOLATED PROPELLER

1. Propeller Operating at Zero Angle of Attack

From the momentum theory of the simplified propeller i.e., the so-called actuator disk(4), (5), (24) one has the following considerations.

a. Flow Field Ahead of the Propeller

By placing a uniform distribution of sinks with strength dispersed over the actuator disk and superimposing the undisturbed uniform flow, the axisymmetrical flow field may easily be solved. Sinks have the strength per unit area of $-\frac{dH}{2\pi r dr} = -a U_\infty$ where the quantity $a U_\infty$ represents the increment of the axial component of the velocity in going through the disk and persisting for locations lying immediately downstream. The value of the quantity a is given by the following relation(4)

$$a = \frac{\Delta p}{2 \rho_\infty U_\infty} = -\frac{1}{2} + \left(\frac{1}{4} + \frac{2C_T}{\pi B^2}\right)^{1/2} \qquad (25)$$

where ΔP is the pressure variation through the propeller
C_T is defined by the thrust relation $T = 4C_T R^2 \rho_\infty U_\infty^2$ where R is the radius of the actuator disk. $\beta^2 = 1 - M_\infty^2$

b. Flow Field Behind the Propeller

By superimposing the flow that consists of a stream having a constant velocity $2a\beta^2 U_\infty$ within the slipstream and a zero velocity outside of it and the flow produced by the above mentioned distribution of sinks, the flow field behind the propeller may be determined. The general solution may be found in Weinig's(6) work. However, for points lying sufficiently far aft of the actuator disk, Ferrari(4) rewrote Koning's formulas(5) for the velocity increments both in the slipstream and outside the slipstream as follows:

$$\left.\begin{aligned} v_x &= aU_\infty \left[1 - 2M_\infty^2 + \frac{x_1}{(R^2 + x_1^2)^{1/2}} \right] \\ \frac{1}{\beta} v_y &= \frac{1}{2} aU_\infty \frac{R^2 y}{(R^2 + x_1^2)^{3/2}} - 2aU_\infty \frac{R_y}{(y^2 + z^2)} \tan\phi \\ \frac{1}{\beta} v_z &= \frac{1}{2} aU_\infty \frac{R^2 z}{(R^2 + x_1^2)^{3/2}} + 2aU_\infty \frac{Ry}{(y^2 + z^2)} \tan\phi \end{aligned}\right\} \quad (26)$$

for $y^2 + z^2 \leq R_1^2$

and

$$\left.\begin{aligned} v_x &= -\frac{1}{2} aU_\infty \frac{R^2 x_1}{(x_1^2 + y^2 + z^2)^{3/2}} \\ \frac{1}{\beta} v_y &= \frac{1}{2} aU_\infty \frac{R^2 y}{(x_1^2 + y^2 + z^2)^{3/2}} \\ \frac{1}{\beta} v_z &= \frac{1}{2} aU_\infty \frac{R^2 z}{(x_1^2 + y^2 + z^2)^{3/2}} \end{aligned}\right\} \quad (27)$$

for $y^2 + z^2 \geq R_1^2$

where $\tan\phi = U_\infty / \omega R$ $x_1 = x/\beta$ and R = the radius of the disk. The coordinate system is chosen as in the following sketch.

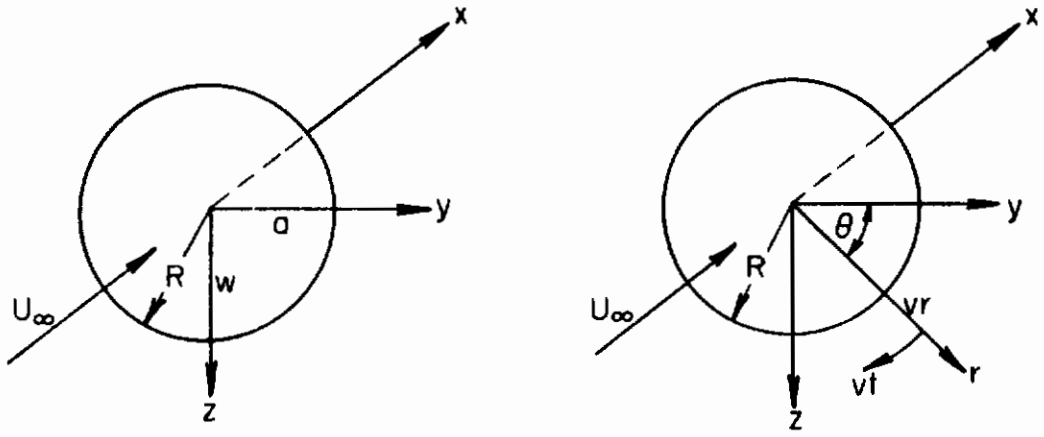

Sketch 12

The boundary of the slipstream is seen to be a body of revolution whose radius R_1 at point x is determined through the equation of continuity (see the following sketch).

$$\pi R_1^2 \rho_1 (U_\infty + v_x) = \pi R^2 U_\infty \left[1 + a(2\beta^2 - 1)\right] \rho_p \qquad (28)$$

where ρ_p is the density of the air immediately behind the propeller.

Introducing the relation for Δp in Eq. (25) and neglecting terms of higher orders in a, we have

$$\frac{\rho}{\rho_p} = 1 + M_\infty^2 \left[a(1 - 2M_\infty^2) - \frac{v_x}{U_\infty} \right] \qquad (29)$$

and then

$$R_1^2 = R \left\{ \frac{1 + a - 2aM_\infty^2}{1 + M_\infty^2 \left[a(1 - 2M_\infty^2) - \frac{v_x}{U_\infty} \right]} \quad \frac{1}{1 + \frac{v_x}{U_\infty}} \right\} \qquad (30)$$

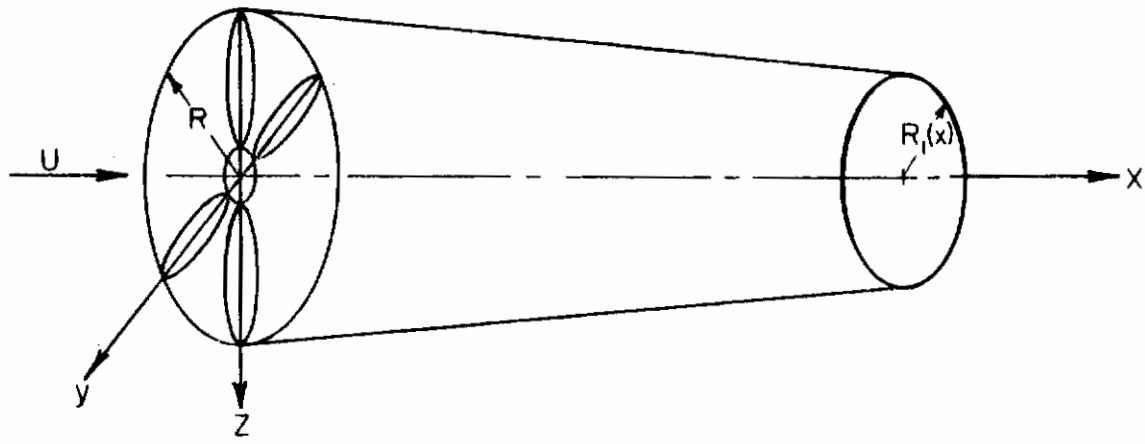

Sketch 13

2. A Propeller Operating at an Angle of Attack α_T

The angle of attack α_T which is the angle between the free stream $\bar{U}_\infty$ and the axis of the propeller is assumed small. Then, the flow field at a large distance from the isolated propeller may be obtained as follows.

In view of the assumptions we made, the axial component of the velocity increment may still be assumed to be the same as in B-1, i.e.,

$$\left.\begin{aligned} v_x &= 2aB^2U_\infty \quad \text{for } y^2+z^2 \leq R_1^2 \\ v_x &= 0 \quad \text{for } y^2+z^2 \geq R_1^2 \end{aligned}\right\} \tag{31}$$

where a is also given by Eq. (25). The velocity increment in the normal direction is given in average value

$$\bar{v}_{z\infty} = \frac{4U_\infty}{(2+a)\pi}(C_z + \alpha_T C_T) \tag{32}$$

where C_z is defined by the equation

$$Z + \alpha_T T = (C_z + \alpha_T C_T)\, 4R^2 \rho_\infty U_\infty^2 \tag{33}$$

where Z is body force in the z-axis direction. Outside the slipstream, the velocity increments in the y and z directions are found by placing a doublet of strength $2\pi R^2 \bar{v}_{z\infty}$ at the center of the circular cross section

of the slipstream. It follows that

$$v_{y\infty} = \bar{v}_{3\infty} \frac{R^2 y z}{(y^2+z^2)^2}$$

and

$$v_{z\infty} = -\bar{v}_{3\infty} \frac{R^2 y^2}{(y^2+z^2)^2} \qquad (34)$$

Although α_T has been assumed small, C_3 is found to be negligible in comparison with $\alpha_T C_T$. Then Eq. (32) may be rewritten as

$$\bar{v}_{3\infty} = \frac{4\alpha_T U_\infty}{(2+a)\pi} C_T = \frac{1+a}{2+a} 2a\alpha_T U_\infty B^2 \qquad (35)$$

and for small values of a this may be further reduced to

$$\bar{v}_{3\infty} = a\alpha_T U_\infty B^2 \qquad (36)$$

Ferrari also derived the equations for velocity increments for points lying closer to the propeller. He then assumed that the real vortex system associated with the propeller may be reduced simply to that of a system of radial bound vortices, lying in the plane of the propeller disk, together with shed trailing vortices having axes aligned parallel to the free stream velocity vector (See Fig. 13). Let $\gamma_p(\theta) R d\theta$ denote the strength of the bound vortices in any sector of the circular system of vortices, where $d\theta$ represents the angular amplitude of the sector in question.

γ_p may be written into two parts as follows:

$$\gamma_p = \gamma_p^{(0)} + \gamma_p^{(1)} \cos\theta \qquad (37)$$

where $\gamma_p^{(1)} = 2\bar{v}_{3\infty}$ and $\gamma_p^{(0)}$ is a constant. Equation (37) shows how the strength of the trailing vortex system varies over the cylindrical surface of the slipstream. Omitting the lengthy derivation given in Ref. 4, we obtain the following relations for v_3.

$$v_3 = \frac{\bar{v}_{3\infty}}{2}(1+A) \text{ for } y \leq R_1$$

and

$$v_3 = -\frac{\bar{v}_{3\infty}}{2}\frac{R^2}{y^2}(1-B) \text{ for } y \geq R_1 \qquad (38)$$

where

$$A = \frac{2x_1}{\pi}\left\{\left(\frac{y^2-2yR-5R^2}{4y^2m}+\frac{m'}{y}\right)K(\alpha)-\frac{Rm'}{y}E(\alpha)\right.$$
$$+\frac{x_1^2+y^2}{y^2}\frac{R}{\left[x_1^2+(y+R)^2\right]^{1/2}}\left[\left(\frac{R}{\sqrt{x_1^2+y^2}}-1\right)\frac{1}{(x_1^2+y^2)^{1/2}+y}\,\Pi(n,k)\right.$$
$$\left.\left.+\left(1+\frac{R}{\sqrt{x_1^2+y^2}}\right)\frac{1}{(x_1^2+y^2)^{1/2}-y}\,\Pi(n',k)\right]\right.$$
$$\left.-\frac{y-R}{y+R}\,\frac{y^2+R^2}{2y^2R}\,\frac{R}{\left[x_1^2+(y+R)^2\right]^{1/2}}\,\Pi(n'',k)\right\} \qquad (39a)$$

and

$$B = \frac{2x_1}{\pi}\left\{\left(\frac{y^2-2yR-5R^2}{4R^2m}+\frac{ym'}{R}\right)K(\alpha)-\frac{ym'}{R}E(\alpha)\right.$$
$$+\frac{x^2+y^2}{R^2}\frac{R}{\left[x_1^2+(y+R)^2\right]^{1/2}}\left[\left(\frac{R}{\sqrt{x_1^2+y^2}}-1\right)\frac{1}{\sqrt{x_1^2+y^2}+y}\,\Pi(n,k)\right.$$
$$\left.\left.+\left(1+\frac{R}{\sqrt{x_1^2+y^2}}\right)\frac{1}{\sqrt{x_1^2+y^2}-y}\,\Pi(n',k)\right]\right.$$
$$\left.-\frac{y-R}{y+R}\,\frac{y^2+R^2}{2R^3}\,\frac{R}{\left[x_1^2+(y+R)^2\right]^{1/2}}\,\Pi(n'',k)\right\} \qquad (39b)$$

where K, E and Π are the complete elliptic integrals of the first, second and third kinds, respectively and

$$m = \frac{1}{2}\left[x_1^2+(y+R)\right]^{1/2}, \quad m' = \frac{m}{yR},$$

$$k^2 = \sin^2\alpha = \frac{4yR}{x_1^2+(y+R)^2}, \quad n = \frac{2y}{y+(x_1^2+y^2)^{1/2}},$$

$$n' = \frac{2y}{(x_1^2+y^2)-y} \quad \text{and} \quad n'' = -\frac{4yR}{(y+R)^2}$$

C. PROPELLER AND WING INTERACTIONS AT SUBSONIC SPEEDS

The propeller-wing interaction problem is divided into two parts; namely, effects produced by the action of the wing upon the propeller and the effects caused by the action of the propeller upon the lifting surface. The alteration of the propeller's aerodynamic characteristics due to the interaction effects is usually insignificant. Therefore, only the latter is treated here.

The resulting flow, when both the propeller and the wing are present, may be decomposed into the following parts:

a) "Undisturbed flow": the uniform flow with velocity V_∞
b) "Propeller flow": the difference between (a) and the flow of the isolated propeller
c) "Airfoil flow": the change in flow caused by the action of the wing when introduced into (a), the propeller being absent
d) "Additional airfoil flow": related directly to the change in circulation around the wing caused by the action of the propeller
e) "Interference flow": the difference between the resulting flow and the flow which consists of (a + b + c + d)
f) "Resulting flow": determined by a superposition of the above subdivisions.

The solutions of parts a), b) and e) are already known (see, for example, Ref. 6). The rest will be discussed in more detail in the following sections.

D. "INTERFERENCE FLOW"

It can be shown that this part of the disturbance flow is contributed by effects of slipstream interaction, i.e., it is equivalent to the wing-body interference problem.

First of all, the conditions to be satisfied at the boundary of the slipstream are:

a) On both sides of the slipstream boundary or surface the pressure should be the same.

b) The perturbation velocity vectors on both sides of the boundary are parallel. In the case of steady flow they are equal to zero.

c) Condition a) is based on the fact that the boundary is a fluid surface, and condition b) is no more than a condition of continuity (see the sketch on the following page).

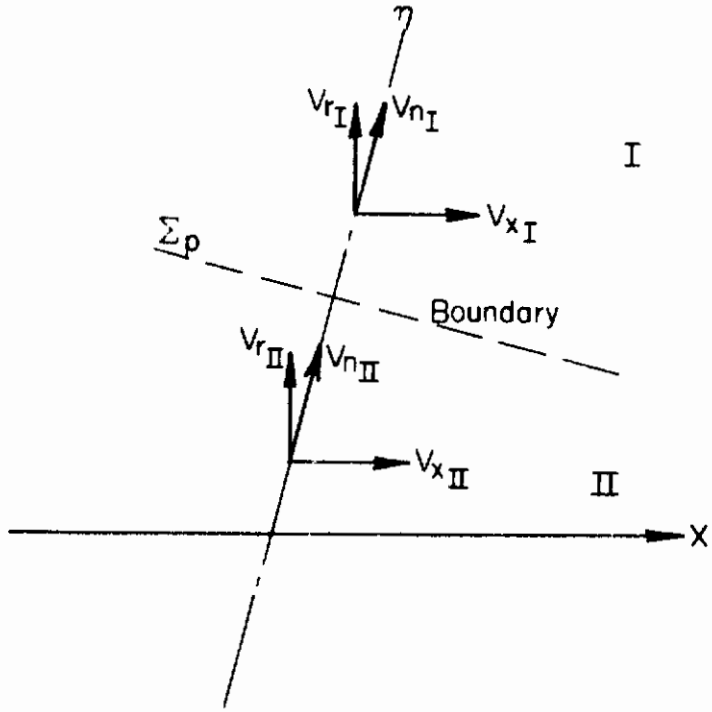

Sketch 14

Boundary conditions a) and b) may be rewritten in the following mathematical forms

$$\rho_I = \rho_{II}, \quad \rho_I = \rho_I \tag{40}$$

and

$$\frac{V_{r_I}}{V_{x_I}} = \frac{V_{r_{II}}}{V_{x_{II}}} \tag{41}$$

Now, let the potential solutions of flow a) and b) in Section C be $\phi_I^{(1)} U_\infty$ and $\phi_{II}^{(1)} U_\infty$ in the region outside and inside of the slipstream, respectively. Similarily, let $\phi_I^{(2)} U_\infty$ and $\phi_{II}^{(2)} U_\infty$ be the solutions for flow c), d) and e). According to previous assumptions, the total resultant flow may be expressed in the following form

$$\phi_I = (\phi_I^{(1)} + \phi_I^{(2)}) U_\infty, \quad \phi_{II} = (\phi_{II}^{(1)} + \phi_{II}^{(2)}) U_\infty \tag{42}$$

A new coordinate system (x', y', z') is defined, which is just a parallel transformation of (x, y, z) with the y' axis coinciding with bound vortex on the lifting surface (see Fig. 14).

The lifting surface, as mentioned previously, is replaced by the lifting line system i.e., "bound vortex" and "trailing vortex" systems $\phi_I^{(1)}$ and $\phi_{II}^{(1)}$ satisfy the boundary condition; therefore the boundary condition may be used to determine the unknown potentials $\phi_I^{(2)}$ and $\phi_{II}^{(2)}$.

1. Condition on the Trailing Vortex Sheet

On the vortex sheet, the discontinuities of potentials $\phi_I^{(2)}$ and $\phi_{II}^{(2)}$ are given in the following forms

$$\left.\begin{aligned} \left(\phi_I^{(2)}\right)_{3'=0^-} - \left(\phi_I^{(2)}\right)_{3'=0^+} &= \frac{\Gamma_I}{U_\infty} \\ \left(\phi_{II}^{(2)}\right)_{3'=0^-} - \left(\phi_{II}^{(2)}\right)_{3'=0^+} &= \frac{\Gamma_{II}}{U_\infty} \end{aligned}\right\} \qquad (43)$$

where Γ_I and Γ_2 are the strengths of the vortices in $R_1 < |y| < b/2$ and $|y| \leq R_1$, respectively. The values of Γ are given by:

$$\Gamma = \frac{1}{2} C_{l_d} c U_\infty \left[\left(1 + \frac{U_I}{U_\infty}\right) \alpha - \left(\frac{\partial \phi}{\partial 3'}\right)_{3'=x'=0} - \alpha_i \right] \qquad (44)$$

where

$$\alpha = \pm \left(\frac{\partial \phi^{(x)}}{\partial 3'}\right)_{\substack{x'=\infty \\ 3'=0}}$$

α = geometric angle of attack

2. Conditions on the Boundary of the Slipstream

The boundary conditions on the fluid surface of revolution of the slipstream as shown in Eqs. (40) and (41) may be reduced to a simpler form if the wing is assumed to lie at a sufficiently large distance from the propeller.

From Eq. (42) and the equations in Section B one has

$$(U_x)_I = U_\infty \left(1 + \frac{\partial \phi_I^{(3)}}{\partial x}\right) \text{ and } (U_x)_{II} = U_\infty \left(1 + 2\alpha\beta^2 + \frac{\partial \phi_{II}^{(2)}}{\partial x}\right) \qquad (45)$$

Since the flow in either Region I or II is assumed to be irrotational, Bernoulli's equation may then be applied. Neglecting the terms of second or higher order in the perturbations produced by the wing, one has

$$\frac{\gamma}{\gamma-1}\frac{p_\infty}{\rho_\infty}+\frac{1}{2}U_\infty^2=\frac{\gamma}{\gamma-1}\frac{p_I}{\rho_I}+\frac{1}{2}\left(1-2\frac{\partial\phi_I^{(2)}}{\partial x}\right) \tag{46}$$

$$\frac{\gamma}{\gamma-1}\frac{p_\infty}{\rho_\infty}+\frac{1}{2}U_\infty^2(1+2aB^2)^2$$

$$=\frac{\gamma}{\gamma-1}\frac{p_{II}}{\rho_{II}}+\frac{1}{2}U_\infty^2(1+2aB^2)^2\left(1+2\frac{\partial\phi_{II}^{(2)}}{\partial x}\frac{1}{1+2aB^2}\right) \tag{47}$$

and also

$$p_I=p_{II}=p_\infty$$

and

$$\rho_I=\rho_{II}=\rho_\infty$$

Therefore one obtains

$$\frac{\partial\phi_I^{(2)}}{\partial x}=S\frac{\partial\phi_{II}^{(2)}}{\partial x} \tag{48}$$

where

$$S=\frac{V_{II}}{V_I}=1+2aB^2$$

Equation (48) may be integrated with respect to x giving

$$\phi_I^{(2)}=S\phi_{II}^{(2)} \tag{49}$$

on the boundary of the slipstream.

From Eq. (41), one has

$$S\frac{\partial\phi_I^{(2)}}{\partial r}=\frac{\partial\phi_{II}^{(2)}}{\partial r}$$

Now, let $\phi^{(2)}$ consist of two parts, designated as Ψ' and Ψ''. Ψ' describes the field of flow induced by the vortex system in the presence of the wing, while Ψ'' gives the additional contribution which is required in order to satisfy the boundary conditions on the slipstream surface.

Following Ferrari(4), one defines a nondimensional form of the circulation as

$$\gamma(y)=\frac{\Gamma(y)}{bU_\infty}$$

Carrying out the method of images and introducing the boundary conditions on S_p, the potential Ψ may be determined at a large distance from the propeller.

$$\left[\phi_\infty^{(2)}\right]=(\Psi_\infty')_I+(\Psi_\infty'')_I=\Psi_\infty'-\frac{(S-1)^2}{1+S^2}(\phi')_{II}-\frac{S^2-1}{1+S^2}(\phi'_\infty)_{II} \tag{50a}$$

and

$$\left[\phi_\infty^{(2)}\right]_{II} = (\Psi_\infty')_{II} + (\Psi_\infty'')_{II} = \Psi_\infty' - \frac{(S-1)^2}{1+S^2}(\Psi_\infty')_I + \frac{S^2-1}{1+S^2}(\Psi_\infty')_{Ir} \qquad (50b)$$

where $(\Psi_\infty')_{IIr}$ and $(\Psi_\infty')_{Ir}$ are the potential functions corresponding to the image vortices within the cross-section of the slipstream at $\mathcal{Z}' = \infty$. At the boundary they satisfy the relationships shown in the sketch below.

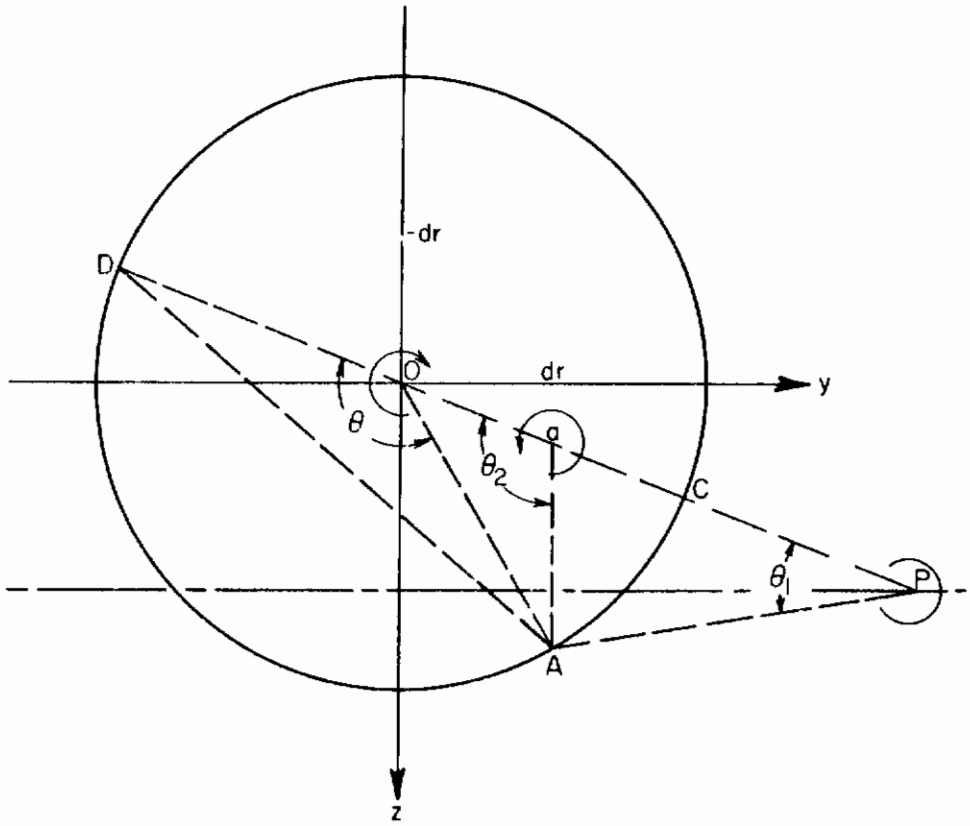

Sketch 15

where $\overline{OP} \cdot \overline{OQ} = \overline{OC}^2$

and $d(\Psi_\infty')_r$ is used to denote the potential corresponding to the vortices running through Q and through D which are related, as explained above to the one passing through P.

Then, from the relation in Eq. (44),

$$(\alpha_i)_I = \frac{1}{2}\left[\frac{\partial \Psi_\infty'}{\partial \mathcal{Z}'} - \frac{(S-1)^2}{S^2+1}\frac{\partial(\Psi_\infty')_I}{\partial \mathcal{Z}'} - \frac{S^2-1}{S^2+1}\frac{(\partial \Psi_\infty')_{IIr}}{\partial \mathcal{Z}'}\right]_{\mathcal{Z}'=0} \qquad (51a)$$

and

$$(\alpha_i)_{II} = \frac{1}{2}\left[\frac{\partial \Psi_\infty'}{\partial \beta'} - \frac{(S-1)^2}{S^2+1}\frac{\partial (\Psi_\infty')_I}{\partial \beta'} - \frac{S^2-1}{S^2+1}\frac{\partial (\Psi_\infty')_{II}}{\partial \beta'}\right]_{\beta'=0} \tag{51b}$$

Discarding terms with a^2, Eqs. (50) and (51) may be written as

$$(\phi_\infty^{(2)})_I = \Psi_\infty' - 2aB^2(\Psi_\infty')_{II} \quad \text{and} \quad (\phi_\infty^{(2)})_{II} = \Psi_\infty' + 2aB^2(\Psi_\infty')_{II} \tag{52}$$

$$\left.\begin{aligned}(\alpha_i)_I &= \frac{1}{2}\left[\frac{\partial \Psi_\infty'}{\partial \beta'} - 2aB^2\frac{\partial (\Psi_\infty')_{II}}{\partial \beta}\right] \\ (\alpha_i)_{II} &= \frac{1}{2}\left[\frac{\partial \Psi_\infty'}{\partial \beta'} + 2aB^2\frac{\partial (\Psi_\infty')_{II}}{\partial \beta'}\right]\end{aligned}\right\} \tag{53}$$

It should be noted that there are three values of S which may be used for checking the results obtained here. For $S=0$ the boundary is the same as a "free jet surface", for $S=\infty$ the boundary is a solid surface, and for $S=1$ there is no boundary.

E. COMPARISON WITH EXPERIMENT

The numerical results of the present theory for the simple case of an elliptic wing are shown in Fig. 15. Plots are presented of ΔC_L and ΔC_D which are determined from the incremental circulation $\Delta\gamma(\eta)$, against the parameters $(S-1)$.

Since no reliable experimental data for the individual components of the additional airfoil flow is available, the comparisons are based on the computed values of the overall effects embodied in the increments ΔC_L and ΔC_D derivable from the formulas in the Appendix, with the corresponding experimentally determined increments in L and D.

The experimental data is based on Possios tests(8) of a trapezoidal planform wing $(AR=6.7)$ operating behind a propeller set at zero angle of attack $\alpha_T=0$. The increments are shown in Figs. 15 and 16. However the theoretical results in the figures are calculated from the equation for an elliptical wing.

Ferrari uses

$$\Delta C_{D_0} = 2(C_{d_0})_\alpha (S_x - 1)$$

which is obtained on the assumption that it is permissible to neglect the small changes produced in the profile drag because of any local changes in

the angle of attack.

This simplified formula is equivalent to a change in the form drag of the entire wing in question, by an amount

$$\Delta C_{D_0} = 2 (C_{d_0})_\alpha (S_r - 1) \frac{A_p}{A}$$

The comparison indicates agreement in the case of the ΔC_D values but the computed values of ΔC_L are somewhat too high to fit the actual test results. The discrepancy seems to be due to the assumption that the disturbances of the slipstream caused by the presence of the lifting surfaces are small. Therefore, Weinig[6] proposed that a correction factor K, where $K = 1/3 + 2/3 \frac{R}{C} \tanh \frac{C}{R}$, be applied to the circulation distribution $\Delta \gamma$ which gives fairly good results.

F. SIMPLIFICATION OF NUMERICAL CALCULATION

From the previous section, it is clear that without introducing an arbitrary correction factor the theory presented above may be only qualitatively correct. However considering all the other assumptions and idealizations made in the theory and bearing in mind the tediousness of the solution for the change in circulation of the part of the airfoil in the slipstream which finally, gives only a second order contribution, one may, for design purposes, eliminate the contribution of flow d, namely, the "additional airfoil flow" and carry out the image process directly from flow c, or the airfoil flow. This simply means that the change in circulation caused by the action of the propeller is identical with that which would result from the propeller-induced change in the angle of attack for the wing located in an undisturbed flow. In other words, one may simply superimpose the local flow angle due to the propeller slipstream onto the local geometric angle of attack; then compute the load for the resultant distribution of angle. Finally, after comparing with the experimental data, some modification of Weinig's correction factor may be introduced, which in turn would give a satisfactory method for fulfilling the design purpose.

G. JET SLIPSTREAM INTERFERENCE

Solutions for the developing flow fields in two-dimensional or circular free jets are available in Ref. 25. Also the solution of a jet of finite width emerging into a uniform stream may be found in Refs. 26 and 27. Shapiro[28] gives linearized solutions for the flow field at the exits of two-dimensional nozzles. However the complete solution of a jet emerging into a disturbed field due to the presence of a wing and body is lacking. However, in order to calculate the effect of a jet exhaust on the wing load distribution it is not necessary to have a detailed solution for the jet flow field. Considering the assumptions made in the previous sections, the following simplifying approximations are made for calculating jet interference effects. The flow field potential of the jet stream must be known.

Here the stream is assumed to have uniform flow with constant cross-section along streamlines. This assumption is partially justified by the above discussion and also seems reasonable because the greater part of the jet interference comes from the neighborhood of the nacelle and lifting surface. In other words, the viscous effect i.e., the turbulent mixing process is ignored.

The velocity potential of the proposed uniform round jet without the presence of wing or body may easily be calculated. Let the potentials of jet stream be $\phi_I^{(1)}$ and $\phi_{II}^{(1)}$ outside and inside of the boundary respectively. The following sketch shows a cross section of the flow

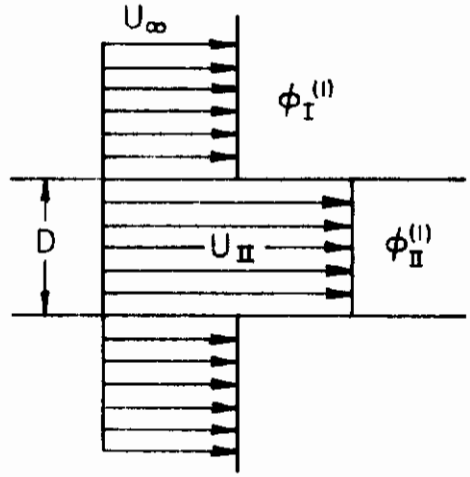

Sketch 16

where D is the diameter of the exit of the nacelle nozzle and U_{II} the speed of the exhaust jet. As in the propeller slipstream case, let $\phi_I^{(2)}$ and $\phi_{II}^{(2)}$ be the solution for flows c), d) and e). (See Section C).

Again the boundary conditions of the slipstream are

$$\rho_I = \rho_{II}$$

and

$$\frac{v_{r_I}}{v_{x_I}} = \frac{v_{r_{II}}}{v_{x_{II}}}$$

The total resultant flow may be expressed in the following form:

$$\phi_I = (\phi_I^{(1)} + \phi_I^{(2)}) \qquad (54)$$

$$\phi_{II} = (\phi_{II}^{(1)} + \phi_{II}^{(2)})$$

The character of the slipstream i.e., the flow (a + b) is assumed to be uninfluenced by the presence of the wing. The lifting surface, whether it intersects the slipstream or not, is replaced by a lifting line

system i.e., the "bound vortex" and "trailing vortex" system. Now, assume that $\phi^{(2)}$ is composed of the two subparts ψ' and ψ'' where ψ' describes the field of flow induced by the vortex system in the presence of the wing and ψ'' gives the additional contribution which is required in order to satisfy the boundary conditions on the slipstream surface.

Introducing the parameter $S = \frac{V_{II}}{V_I}$ and the boundary conditions the image process may be carried out as in Section C.

Here a simple case is treated. The lifting surface is assumed not intersecting the jet slipstream; then, the image process is simplified.

The potential of a flow around a line vortex through the point $y = y_1$, $z = 0$ with a circulation strength Γ is:

$$\phi_1 = \frac{\Gamma}{2\pi} \tan^{-1} \frac{z}{y - y_1} \tag{55}$$

After introducing the boundary conditions and the image method the potential of the additional flow is found to be

$$\left.\begin{aligned} \psi_I'' &= -\frac{S^2-1}{S^2+1}\,\phi_2 + \frac{S^2-1}{S^2+1}\,\phi_3 \qquad (r \geq R) \\ \psi_{II}'' &= -\frac{(S-1)^2}{S^2+1}\,\phi_1 \qquad\qquad\quad (r \leq R) \end{aligned}\right\} \tag{56}$$

where

$$\phi_2 = \frac{\Gamma}{2\pi} \tan^{-1} \frac{z}{y - R^2/y_1}$$

and

$$\phi_3 = \frac{\Gamma}{2\pi} \tan^{-1} \frac{z}{y}$$

It should be noted that ϕ_3, which is the potential for the flow around a vortex situated on the x-axis, is of no practical importance and may be neglected.

Once the additional flow or the so-called interference flow is obtained, the corresponding induced downwash at control points on the wing may be determined. Finally the resulting linear aerodynamic load distribution may be calculated by the methods described in Ref. 1.

It should be noted that the turbulent mixing process begins at the exit of the engine nozzle. A typical profile of the jet wake is shown in Fig. (17). Consequently, the pressure equalization and the angle of attack of the jet with respect to the stream, if any, can have a profound effect on the shape of the wake. A jet wake draws air particles from the ambient air i.e., the ambient air becomes involved in the wake and increases its mass flow, the amount of entrained air increasing gradually with distance from the exit. When a lifting surface is situated in a region that is affected by the wake, the change in stream direction

due to ambient air entrainment produces a change in downwash over the surface. This change in downwash varies with the angle of incidence and jet velocity, and influences the stability of the aircraft. Details of this and the important temperature distribution in the wake are beyond the scope of the present investigation. Some information may be found in Refs. 27 to 30.

H. DISCUSSION ON NONUNIFORMITY

Both in the present case and in the wing-tail interference calculation, the changes in circulation on the lifting surfaces due to the nonuniformity of the oncoming flow are neglected. In other words, it is assumed that the contribution of the nonuniformity on the aerodynamic load may be accounted for by modifying relevant local angles of attack or by suitably transforming the local coordinates. However this simplification may only be valid for a very small nonuniformity in the oncoming flow. The first order approximation may be added if it is seen necessary. The method given in the Appendix may be used to calculate the change in circulation due to a nonuniformity which is introduced by forward components such as propeller, lifting surface, bodies etc. in the oncoming flow, provided the disturbances i.e., the perturbations of velocity components v_x, v_y, v_z, are small compared to the undisturbed free stream velocity v_∞ and are proportional to some parameters which characterize the different cases. In the propeller slipstream interference problem, the parameter is a (Eq. (25)) and the circulation may be expressed as follows:

$$\Gamma = \Gamma_0 + \Gamma_1 a + \Gamma_2 a^2 + \cdots$$

The procedures described in the Appendix permit calculation of the value of Γ_1 and therefore the first-order approximation of the change in circulation may be added in the total solution.

APPENDIX

CALCULATION OF THE CHANGE IN CIRCULATION

The lifting surface is assumed to traverse the slipstream at a large distance aft of the propeller. Following Muggin[7] and Ferrari[4] the relations for the special case of the lifting line passing diametrically through the center of the slipstream may be rewritten as follows:

First of all, nondimensionalizing Eq. (44) with the relation $\gamma(y) = \frac{\Gamma(y)}{bU_\infty}$,

$$\gamma = \frac{1}{2}\,\frac{1}{b}\,c_{l_\alpha}\,c\left[\alpha\left(1+\frac{v_x}{U_\infty}\right) - E_p - \alpha_i\right] \tag{A-1}$$

where

$$\left.\begin{aligned} \frac{v_x}{U_\infty} &= 2aB^2 \quad \text{for } |y| \leq R_1 \\ \frac{v_x}{U_\infty} &= 0 \quad \text{for } |y| \geq R_1 \end{aligned}\right\} \tag{A-2}$$

and

$$E_p = (E_p)_{|y|\geq R_1} = \frac{-4}{\pi(2+a)}\,(C_J + \alpha_T C_T)\,\frac{h^2}{\eta^2}$$

where

$$h = \frac{2R_1}{b} \quad \text{and} \quad \eta = \frac{2y}{b}$$

It should be noted again that C_J and C_T are defined by the relation between the velocity increments normal to $\vec{U}_\infty$ and the thrust vector $\vec{T}$. This relation is shown in the following equations

$$\pi R^2 \rho_\infty U_\infty (2+a) v_{J_\infty} = Z + \alpha_T T = (C_J + \alpha_T C_T)\,4R^2\rho_\infty U_\infty^2$$

where Z is the external force in the direction of $\vec{Z}$. Finally, α_i is given by Eq. (53). Now since the pressure or the lift is continuous over the lifting surface, the circulation γ must have a discontinuity at the intersection of the wing and the slipstream, ($J = 0$ in this case) i.e., at $|\eta| = h$. From Eqs. (43) and (49) one has

$$\Delta\gamma = (\gamma_I - \gamma_{II})_{|\eta|=h} = \frac{s-1}{s}\,(\gamma_I)_{|\eta|=h} \tag{A-3}$$

Accordingly, $\frac{d\gamma}{d\eta}$ is also discontinuous at $|\eta| = h$ and the jump is

$$\Delta\left(\frac{d\gamma}{d\eta}\right) = \left(\frac{d\gamma_I}{d\eta} - \frac{d\gamma_{II}}{d\eta}\right)_{|\eta|=h} = -(S-1)\left(\frac{d\gamma_I}{d\eta}\right)_{|\eta|=h} \qquad \text{(A-4)}$$

Let $\gamma = \gamma_d + \gamma_c$

where γ_d is to incorporate the discontinuities $\Delta\gamma$ and $\Delta\left(\frac{d\gamma}{d\eta}\right)$ as defined by Eqs. (A-3) and (A-4), and γ_c is the part of the circulation distribution which is continuous, with continuous first derivative, throughout the whole interval.

Then one has

$$\left.\begin{aligned} \gamma_d &= 0 && \text{for } |\eta| > h \\ \gamma_d &= -a_1 - a_2\eta^2 && \text{for } |\eta| < h \end{aligned}\right\} \qquad \text{(A-5)}$$

now let

$$\gamma_c = \frac{2}{m+1}\sum_{n=1}^{m}\gamma_n \sum_{\mu=1}^{m} \sin\mu\theta_n \sin\mu\theta + a_t \sum_{\mu=1}^{\infty} B_\mu \sin\mu\theta \qquad \text{(A-6)}$$

where $\cos\theta = \eta$, $\theta_n = \frac{n\pi}{m+1}$ and a_1 , a_2 , a_t and the various γ_n' are constants that are apriori unknown. The B values may be found from the following equations

$$B_1 = -\frac{4}{\pi}(2\theta_0 - \pi - \sin 2\theta_0)$$

$$B_\mu = \frac{8}{\pi}\frac{1}{\mu}\left[\frac{-\sin(\mu-1)\theta_0}{\mu-1} + \frac{\sin(\mu+1)\theta_0}{\mu+1}\right] \text{ for } \mu = 3, 5, 7 \text{ etc.}$$

where $\cos\theta_0 = h$

It should then be noted that

$$\sum_{\mu=1}^{\infty} B_\mu \sin \mu\theta = \frac{4\alpha_L}{\pi}\left[(\cos\theta + \cos\theta_0) \ln \frac{\cos\frac{\theta-\theta_0}{2}}{\left|\cos\frac{\theta+\theta_0}{2}\right|} + \pi \sin\theta - (\cos\theta - \cos\theta_0) \ln \frac{\sin\frac{\theta+\theta_0}{2}}{\left|\sin\frac{\theta-\theta_0}{2}\right|}\right]$$

Now Eq. (A-1) must be satisfied at the m points having the coordinates $\eta_n = \cos\theta_n$ where $n = 1, 2 \cdots m$. This leads to the following equations

$$\left.\begin{aligned} &\left(A_{\nu\nu} + \frac{2b}{Cl_\alpha c_\nu}\right)\gamma_\nu + \frac{2b}{Cl_\alpha c_\nu}\alpha_L \sum_{\mu=1}^{\infty} B_\mu \sin\mu\theta_\nu + \sum_{n=1}^{m}{}' A_{\nu n}\gamma_n \\ &+ M_\nu a_2 + M'_\nu = \alpha_\nu - (E_p)_I \quad \text{for } |\eta_\nu| > h \end{aligned}\right\}$$

and

$$\left.\begin{aligned} &\left(B_{\nu\nu} + \frac{2b}{Cl_\alpha c_\nu}\right)\gamma_\nu + \frac{2b}{Cl_\alpha c_\nu}\alpha_L \sum_{\mu=1}^{\infty} B_\mu \sin\mu\theta_\nu + \sum_{n=1}^{m}{}' B_{\nu n}\gamma_n + N_\nu a_2 \\ &+ N'_\nu - \frac{2b}{Cl_\alpha c_\nu}(a_1 + a_2\eta_\nu^2) + 2\alpha_L = \alpha_\nu S - (E_p)_I \quad \text{for } |\eta_\nu| < h \end{aligned}\right\} \quad \text{(A-7)}$$

where the various coefficients are defined below in terms of the Multhopp coefficients $b_{\nu\nu}$ and $b_{\nu n}$ where

$$b_{\nu\nu} = \frac{m+1}{4\sin\theta_\nu}$$

$$b_{\nu n} = \frac{\sin\theta_n}{(m+1)(\cos\theta_n - \cos\theta_\nu)^2} \quad \text{for } |n-\nu| = 1, 3, 5.$$

and

$$b_{\nu n} = 0 \quad \text{for } |n-\nu| = 2, 4, 6.$$

and the factors

$$C = \frac{S^2-1}{1+S^2} \quad \text{and} \quad D = \frac{(S-1)^2}{1+S^2}$$

The coefficients are

$$A_{\nu\nu} = b_{\nu\nu} + \frac{1}{\pi(m+1)} \sum_{\mu=1}^{m} \mu \sin \mu\theta_\nu \left[D I'_{\mu\nu} + C\left(J_{\mu\nu} + J''_{\mu\nu}\right) \right]$$

$$A_{\nu n} = -b_{\nu n} + \frac{1}{\pi(m+1)} \sum_{\mu=1}^{m} \mu \sin \mu\theta_n \left[D I'_{\mu\nu} + C\left(J_{\mu\nu} + J''_{\mu\nu}\right) \right]$$

$$B_{\nu\nu} = b_{\nu\nu} + \frac{1}{\pi(m+1)} \sum_{\mu=1}^{m} \mu \sin \mu\theta_\nu \left[D\left(I_{\mu\nu} + I''_{\mu\nu}\right) - C J'_{\mu\nu} \right]$$

$$B_{\nu n} = -b_{\nu n} + \frac{1}{\pi(m+1)} \sum_{\mu=1}^{m} \mu \sin \mu\theta_\nu \left[D\left(I_{\mu\nu} + I''_{\mu\nu}\right) - C J'_{\mu\nu} \right]$$

$$M_\nu = \frac{2h}{\pi}(1-D) + \frac{\eta_\nu}{\pi}(1-D) \ln \left| \frac{\eta_\nu - h}{\eta_\nu + h} \right|$$

$$M'_\nu = \frac{\alpha k}{2\pi} \sum_{\mu=1}^{\infty} \mu B_\mu \left[D I'_{\mu\nu} + C\left(J_{\mu\nu} + J''_{\mu\nu}\right) \right]$$

$$N_\nu = \frac{2h}{\pi} + \frac{\eta_\nu}{\pi} \ln \left| \frac{\eta_\nu - h}{\eta_\nu + h} \right| - \frac{2Ch^3}{\pi \eta_\nu^2} - \frac{Ch^4}{\pi \eta_\nu^3} \ln \left| \frac{\eta_\nu - h}{\eta_\nu + h} \right|$$

$$N'_\nu = \frac{\alpha k}{2\pi} \sum_{\mu=1}^{\infty} \mu B_\mu \left[D\left(I_{\mu\nu} + I''_{\mu\nu}\right) - C J'_{\mu\nu} \right]$$

where

$$\left.\begin{aligned} J_{\mu\nu} &= \int_0^{\theta_0} \frac{\cos \mu\theta' \cos\theta'}{\cos\theta' \cos\theta_\nu - \cos^2\theta_0} \, d\theta' \\ I_{\mu\nu} &= \int_0^{\theta_0} \frac{\cos \mu\theta'}{\cos\theta_\nu - \cos\theta'} \, d\theta' \end{aligned}\right\} \qquad (A\text{-}7)'$$

The symbols to which primes and double primes have been added are to stand for the same integrals when taken between the limits of θ_0 and $\pi - \theta_0$ in the first instance, and between $\pi - \theta_0$ and π in the second instance.

Equation (A-7) gives a set of $(m+1)/2$ equations containing unknowns $(m+1)/2$ of γ_ν and three unknown constants a_1, a_2 and α_k. If h happens to equal one of the η_ν values from Eq. (A-7) then

$$\frac{1}{\pi(m+1)} \sum_{n=1}^{m} \gamma_n \sum_{\mu=1}^{m} \mu \sin \mu\theta_n \left[D(I^{*}_{\mu,0} - I^{'*}_{\mu,0} + I^{''*}_{\mu,0}) \right]$$

$$- C \left[J^{*}_{\mu,0} + J^{'*}_{\mu,0} + J^{''*}_{\mu,0} \right] + a_2 \left[N^{*}(h) - M^{*}(h) \right] \qquad \text{(A-8)}$$

$$+ \frac{ak}{2\pi} \sum_{\mu=1}^{\infty} \mu B_\mu \left[D(I^{*}_{\mu,0} - I^{'*}_{\mu,0} + I^{''*}_{\mu,0}) \right] - C (J^{*}_{\mu,0} + J^{'*}_{\mu,0} + J^{''*}_{\mu,0})$$

$$+ 2\alpha_k - \frac{2b}{C l_\alpha C_0} (a_1 + a_2 h^2) = a_0 (S-1) - \left[(E_p)_{II} - (E_p)_{I} \right]_0$$

where

$(\ )^{*}$ = the finite part of the quantity is to be evaluated for the case where $\theta = \theta_0$ and $a_0 = \alpha(h)$ $(E_p)_I = (E_p)_I(h)$ etc.

Equations (A-3) and (A-4) may be rewritten in the following form

$$(a_1 + a_2 h^2) \frac{S}{S-1} = \frac{2}{m+1} \sum_{n=1}^{m} \gamma_n \sum_{\mu=1}^{m} \sin \mu\theta_n \sin \mu\theta_0 + \alpha_k \sum_{\mu=1}^{\infty} B_\mu \sin \mu\theta_0$$

and (A-9)

$$\frac{2 a_2 h}{S-1} = \frac{2}{m+1} \sum_{n=1}^{m} \gamma_n \sum_{\mu=1}^{m} \mu \sin \mu\theta_n \frac{\cos \mu\theta_0}{\sin \theta_0} + \alpha_k \sum_{\mu=1}^{\infty} \mu B_\mu \frac{\cos \mu\theta_0}{\sin \theta_0} \qquad \text{(A-10)}$$

Finally Eqs. (A-7), (A-8), (A-9) and (A-10) comprise a set of $\left[\frac{m+1}{2} + 3\right]$ equations for the same number of unknowns, namely γ_η, a_1, a_2 and α_k. Solving these equations gives the distribution of circulation over the lifting surface in the presence of a propeller or the so-called "additional airfoil flow".

REFERENCES

1. Schindel, L. H., An Evaluation of Procedures for Calculating Aerodynamic Loads, M. I. T. Aerophysics Lab. TR 103, 1963.

2. Borland, C. J. Methods of Calculating Aerodynamic Loads on Aircraft Structures: Part I – Wing-Body Interference Effects, Air Force Flight Dynamics Laboratory Technical Report 66-37, January, 1966.

3. Chamberlain, T. E., Methods of Calculating Aerodynamic Loads on Aircraft Structures: Part II – Nonlinear Effects, Air Force Flight Dynamics Laboratory Technical Report 66-37, April 1966.

4. Ferrari, C., "Interaction Problems" Section C of Aerodynamic Components of Aircraft at High Speeds, Edited by A. F. Donovan and H. R. Lawrence, Vol. VII of High Speed Aerodynamics and Jet Propulsion, Princeton University Press, 1957.

5. Koning, C., "Influence of the Propeller on Other Parts of the Airplane Structure", Aerodynamic Theory Vol. IV, Division M. W. F. Durand, Editor-in Chief, Berlin, Julius Springer, (1937).

6. Weinig, F., Aerodynamik der Luftschraube, Springer, Berlin, 1940. Available in English translation from Air Documents Division Intelligence Department, U. S. Air Material Command, Dayton 366-369, (1947).

7. Muggin, A., Sul calcolo dell'interferenza elica-ala (On the Calculation of Propeller-Wing Interference) att. accad. nazl. Lincei, Rome. 11 53-57, (1951).

8. Possio, C., Ricerche sperimentali sull'interferenza elica-ala (Experimental Investigation of Propeller-Wing Interference) Aerotecnia 26 73-7711966.

9. Lagerstrom, P. A. and Graham, M. E., Aerodynamic Interference in Supersonic Missiles, Douglas Aircraft Co. Report SM-13743, July 1950.

10. Spreiter, J. R. and Sacks, A. H., "The Rolling Up of the Trailing Vortex Sheet and It's Effects on the Downwash Behind Wings", J. Aero. Sci., January 1951.

REFERENCES (Continued)

11. Schindel, L. H., Wing-Tail Interference at Supersonic Speeds, Naval Supersonic Laboratory, M. I. T. TR No. 8, (1953).

12. Johnson, B. H., Jr., and Rollins, F. W., Investigation of a Thin Wing of Aspect Ratio 4 in The Ames 12-Foot Pressure Wind Tunnel V-Static Longitudinal Stability and Control Throughout the Supersonic Speed Range of a Semi-Span Model of a Supersonic Airplane, NACA RM No. A9I01, (1949).

13. Brown, C. E. "Aerodynamics of Bodies at High Speeds" Section B of Aerodynamic Components of Aircraft at High Speeds, Edited by A. F. Donovan and H. R. Lawrence, Vol. II of High Speed Aerodynamics and Jet Propulsion, Princeton University Press, 1957.

14. Chen, C. F. and Clarke, J. H., "Body Under Lifting Wing", J. Aero. Sci. Vol. 28, No. 7, July 1961.

15. Smith, N. F. and Carlson, H. W., The Origin and Distribution of Supersonic Store Interference from Measurement of Individual Forces on Several Wing-Fuselage-Store Configurations II – Swept-Wing Heavy-Bomber Configurations with Large Store (Nacelle) Lateral Forces and Pitching Moments: Mach Number, 1.61, NACA RM L55E26a, (1955).

16. Guy, L. D., Load on External Stores at Transonic and Supersonic Speeds, NACA RM L55E136, (1955).

17. Morris, O. A., The Origin and Distribution of Supersonic Store Interference from Measurement of Individual Forces on Several Wing-Fuselage-Store Configurations IV-Delta-Wing Heavy-Bomber Configuration with Large Store: Mach Number, 1.61, NACA RM L55I27a, (1955).

18. Bobbitt, P. J., Carlson, H. W. and Pearson, H. O., Calculation of External-Store Loads and Correlation with Experiment, NACA RM L57DS0a, (1957).

19. Swihart, J. M., Mercer, C. E. and Norton, H. T., Jr., Effect of Afterbody-Ejector Configurations on the Performance at Transonic Speeds of a Pylon-Supported Nacelle Model Having a Hot-Jet Exhaust, NASA Memo 1-4-59L, (1959).

20. Wollner, B. C., An Analysis of Available Data on Effects of Wing-Fuselage-Tail and Wing-Nacelle Interference on the Distribution of the Air Load Among Components of Airplanes, NACA RM No. L9B10 (1949).

REFERENCES (Concluded)

21. Carlson, H. W. and Geier, D. J., The Origin and Distribution of Supersonic Store Interference from Measurement of Individual Forces on Several Wing-Fuselage-Store Configurations V-Swept-Wing Heavy-Bomber Configuration with Large Store (Nacelle) Mach 2.01, RM L55K15, (1956).

22. Runckel, J. F. and Swihart, J. M., A Hydrogen Peroxide Hot-Jet Simulator for Wind-Tunnel Tests of Turbojet Exit Models, NASA Memo 1-10-59L, (1959).

23. Runckel, J. F., Preliminary Transonic Performance Results for Solid and Slotted Turbojet Nacelle Afterbodies Incorporating Fixed Divergent and Jet Nozzles Designed for Supersonic Operation, NASA Memo 10-24-58L, (1958).

24. Rauscher, M., Introduction to Aeronautical Dynamics, John Wiley and Sons, Inc., (1953).

25. Schlichting, H., Boundary Layer Theory, Fourth Edition, McGraw-Hill Book Co. Inc., (1960).

26. Kuethe, A. M., "Investigations of the Turbulent Mixing Regions Formed by Jets", Jour. Appl. Mech. 2, A87-95, (1935).

27. Squire, H. B. and Trouncer, J., Round Jets in a General Stream, ARC 1974, (1944).

28. Forstall, W., Jr., and Shapiro, A. H., Momentum and Mass Transfer in Coaxial Gas Jets, M. I. T. Meteor Report No. 39, (1949).

29. Huff and Abdalla, Mixing Characteristics Downstream of Core Region of High-Temperature Axisymmetric Jets Exhausting into Transonic and Supersonic Streams, NACA TM X-151, (1960).

30. Rousso, M. D. and Banghman, L. E., Spreading Characteristics of a Jet Expanding from Choked Nozzles at Mach 1.91, NACA TN 3836, (1956).

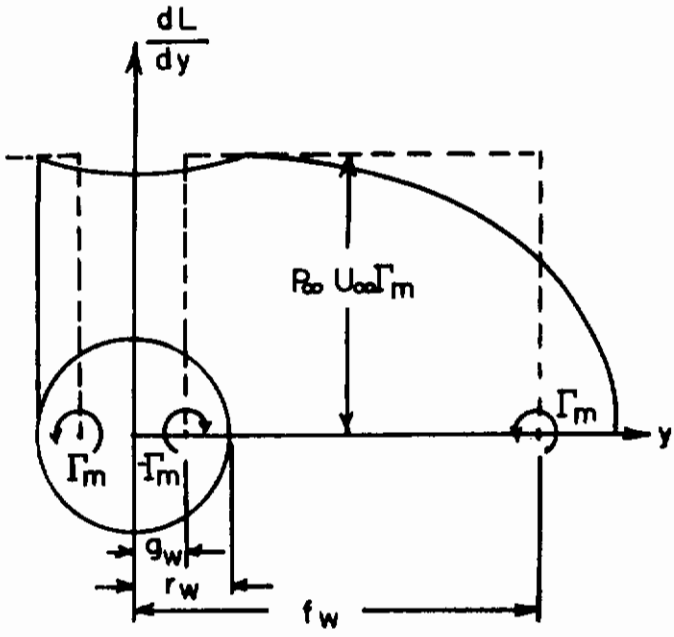

Figure 1. Lift Distribution and Equivalent Vortex System

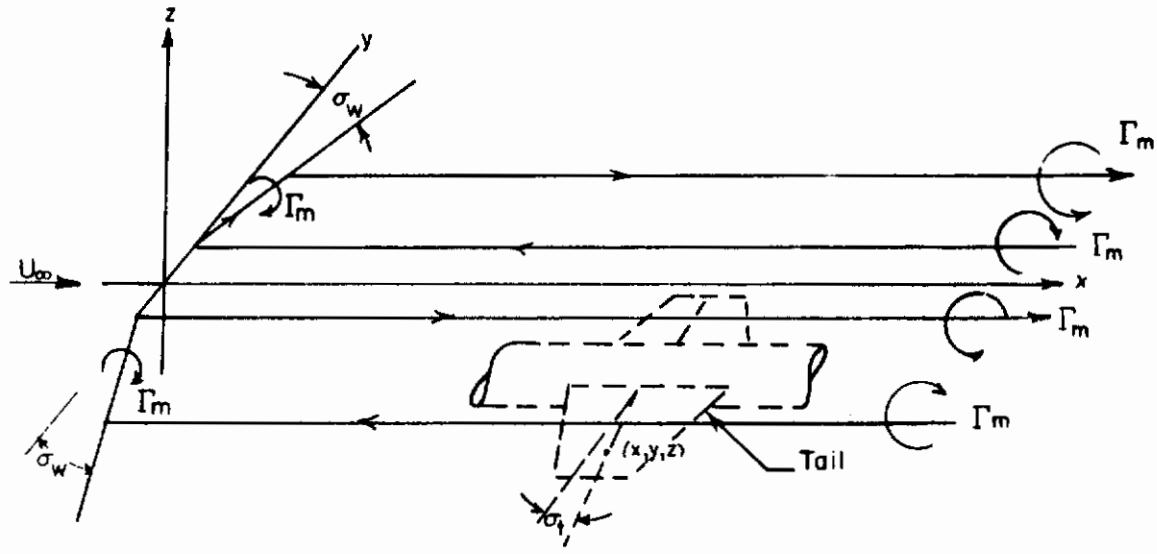

Figure 2. Horseshoe Vortex System

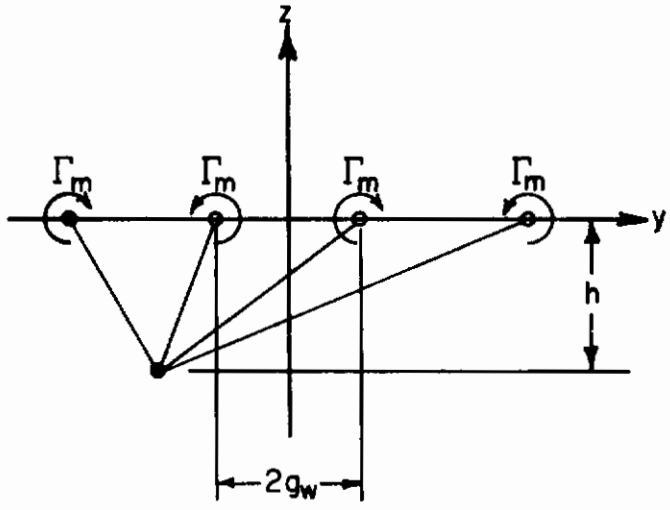

Figure 3. Coordinate System

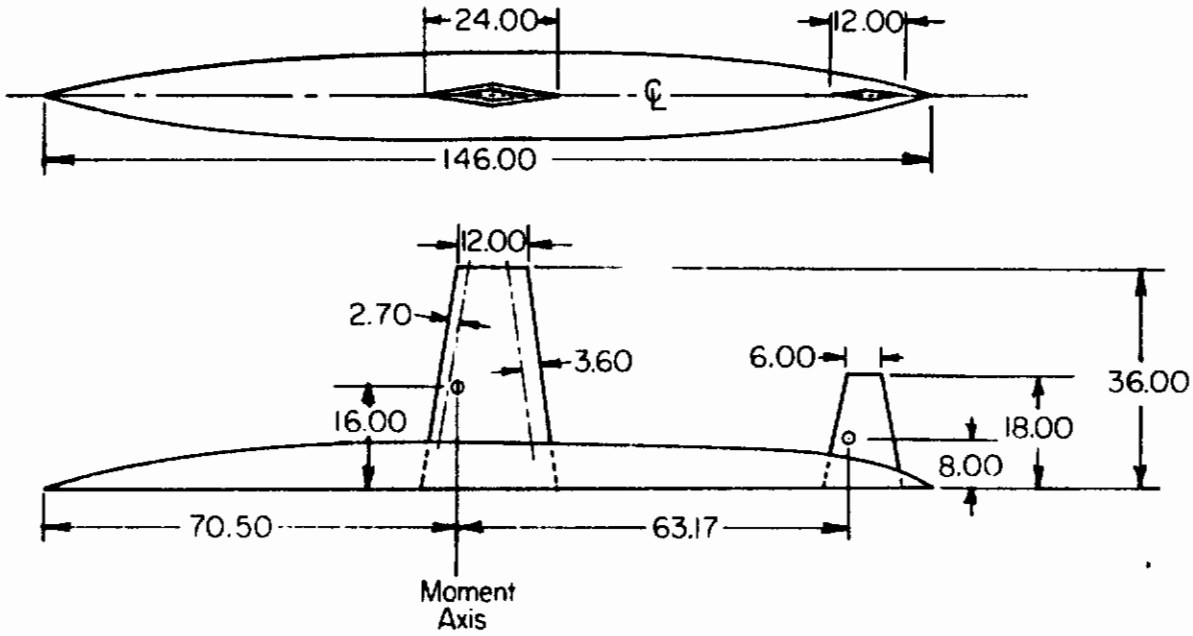

Figure 4. Airplane Configuration

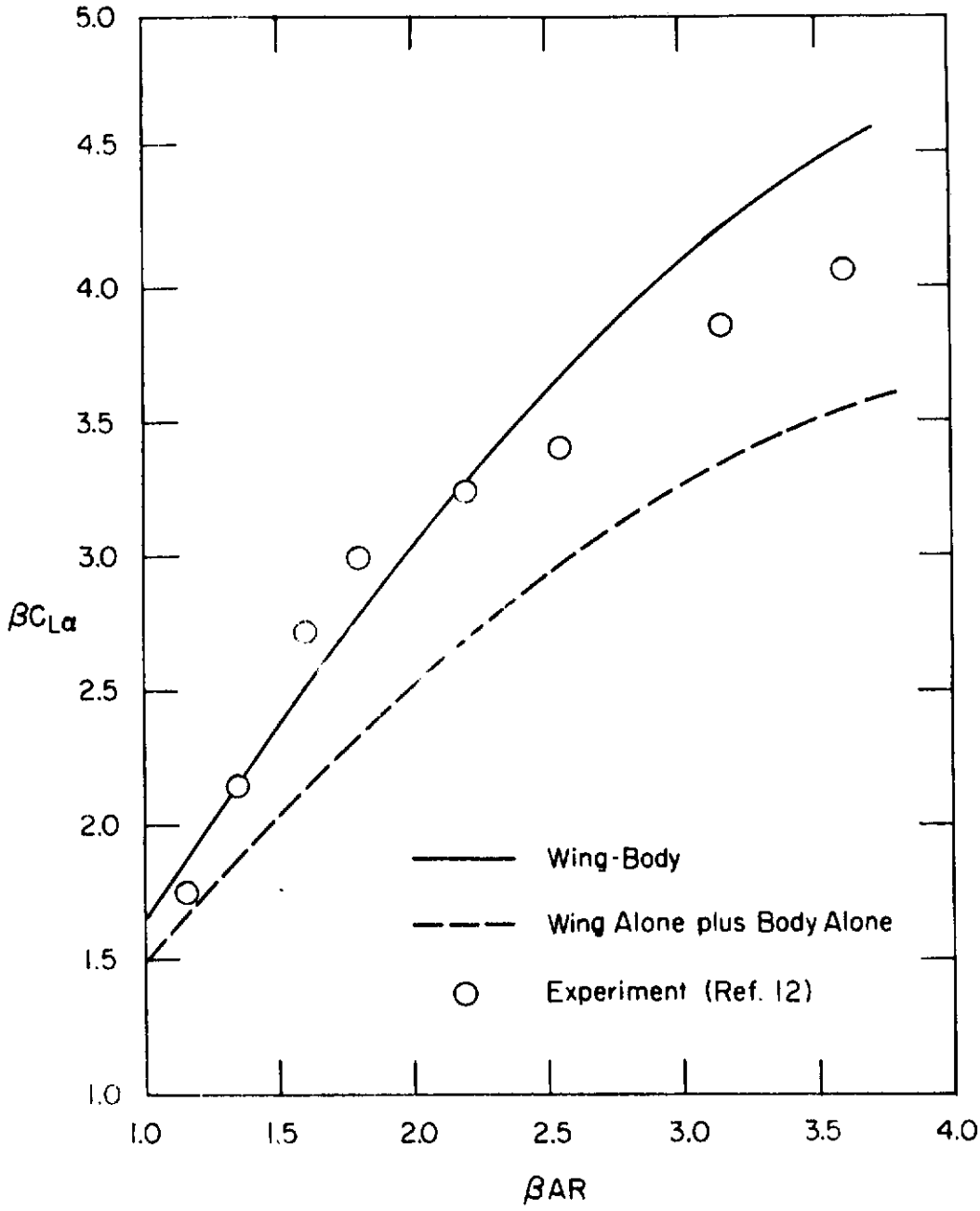

Figure 5. Comparison of Calculated Lift on Wing-Body Combination with Experiment

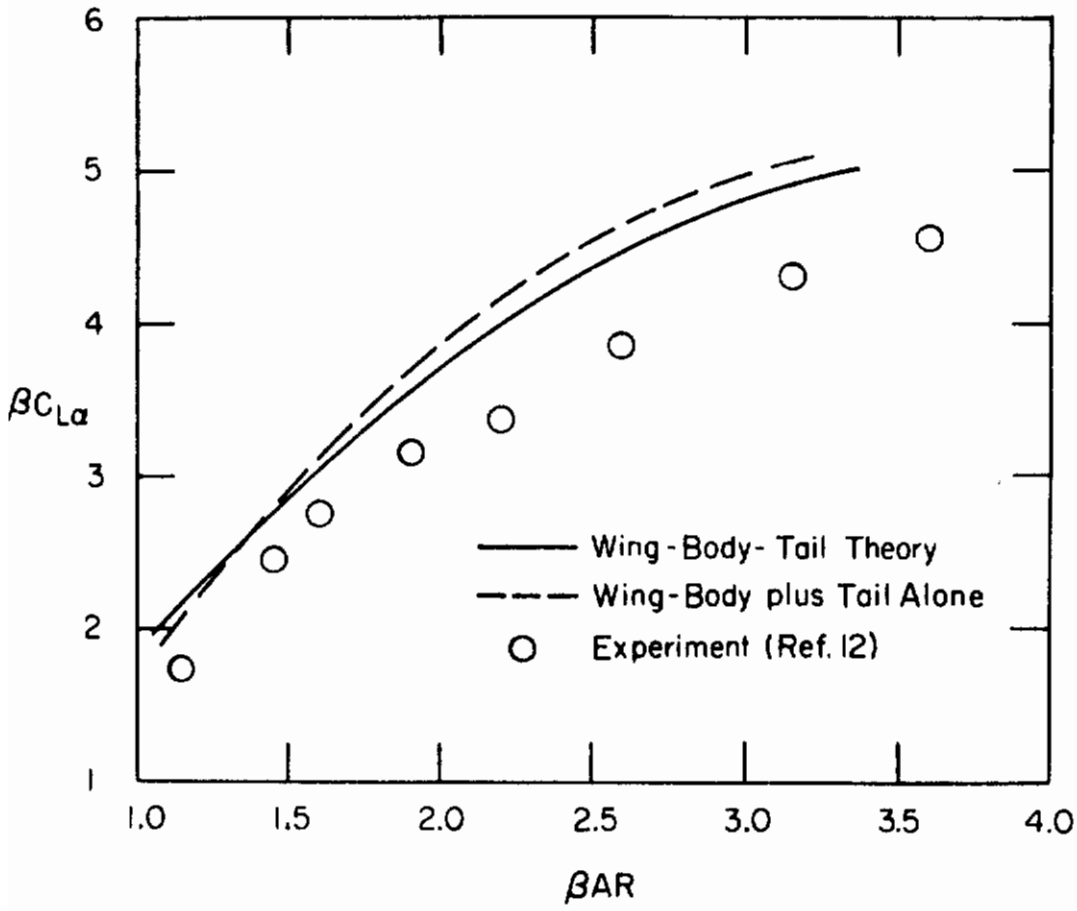

Figure 6. Comparison of Calculated Lift on Wing-Body-Tail Combination with Experiment

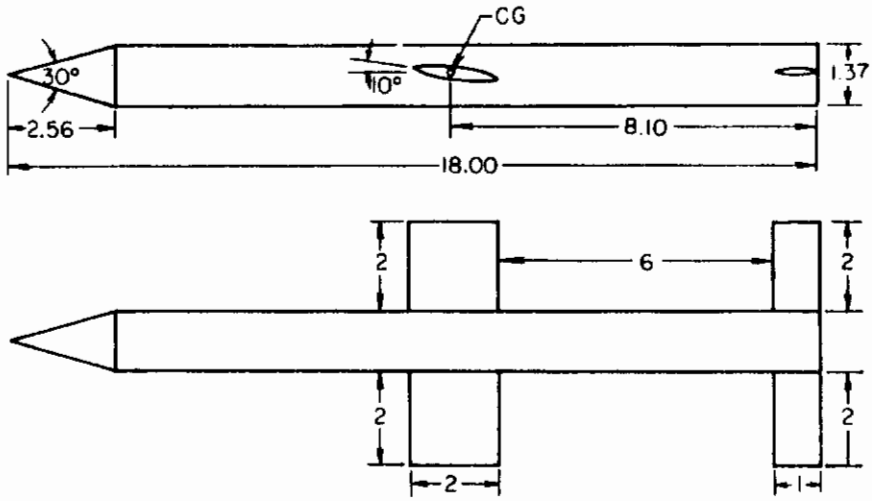

Figure 7a. Missile Configuration

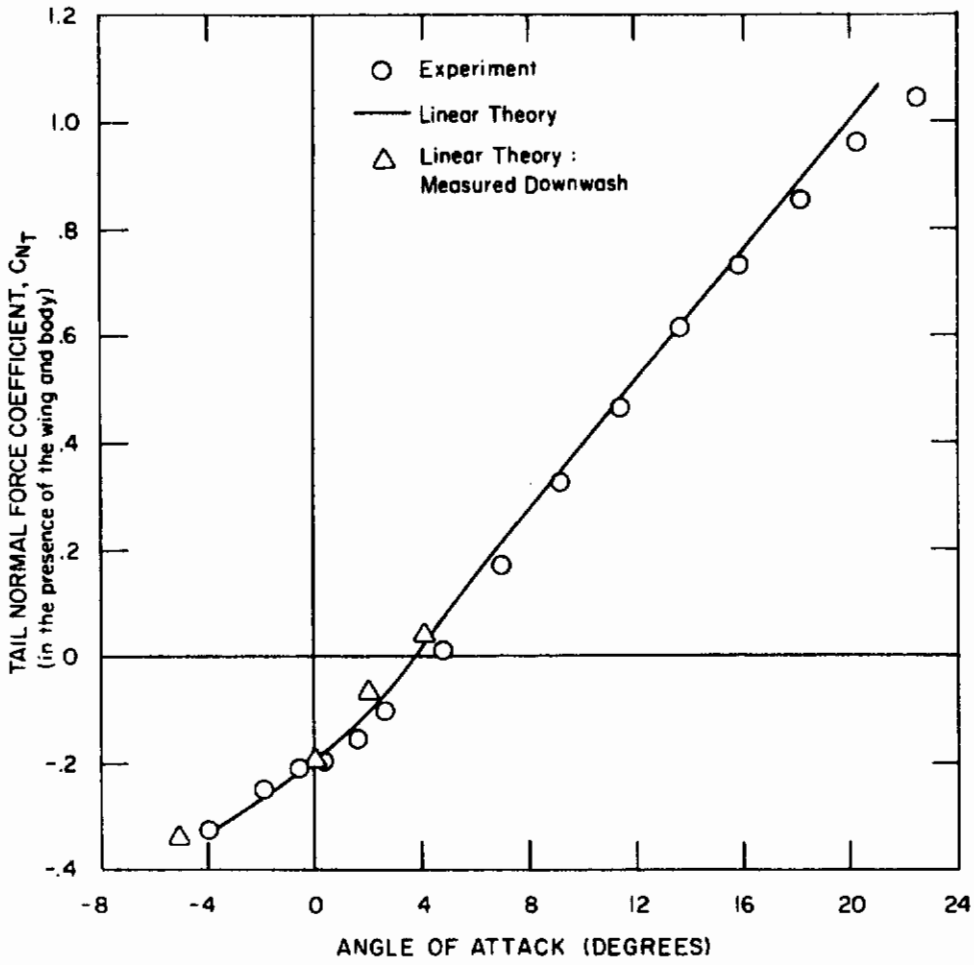

Figure 7b. Comparison of Theoretical and Experimental Normal Force Coefficient on Tail in Presence of Wing and Body

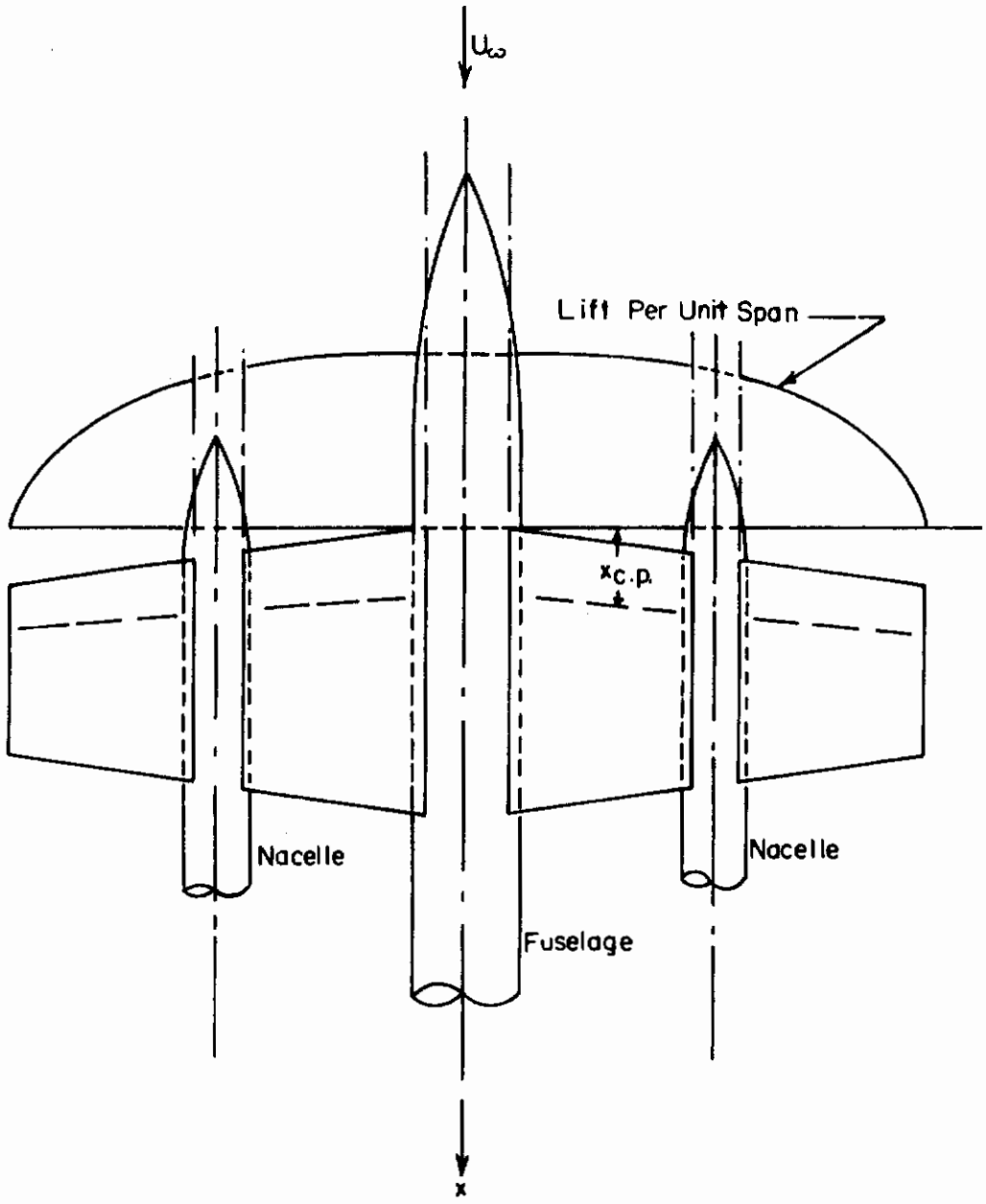

Figure 8. The Spanwise Loading on the Modified Wing

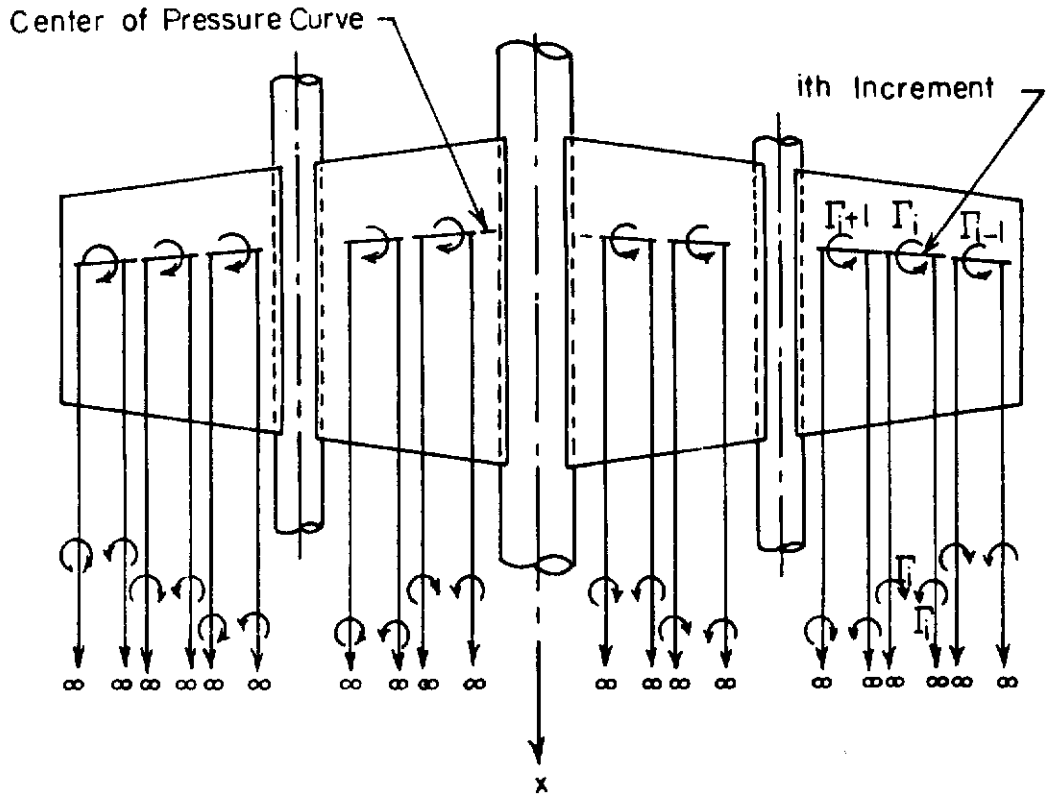

Figure 9. The Trailing Vortex System of the Wing-Body-Nacelle Combination

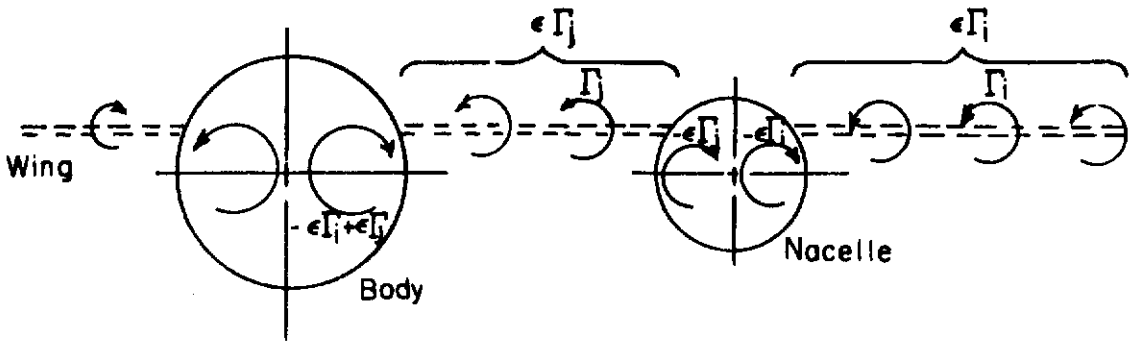

Figure 10. Image Vortex System Due to Right Wing Vortices

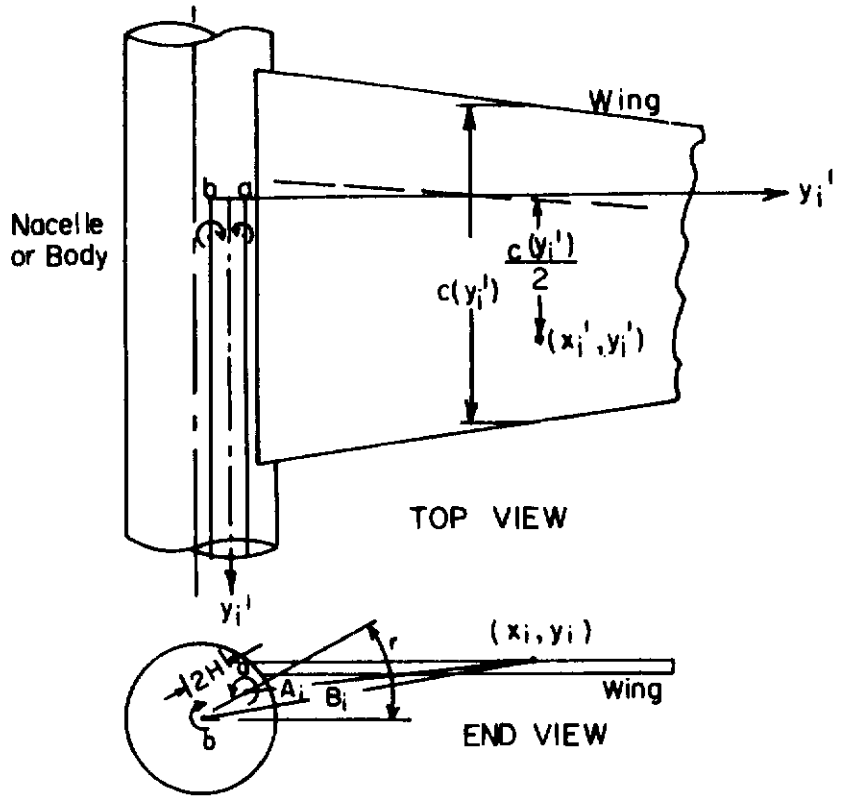

Figure 11. Downwash Calculation

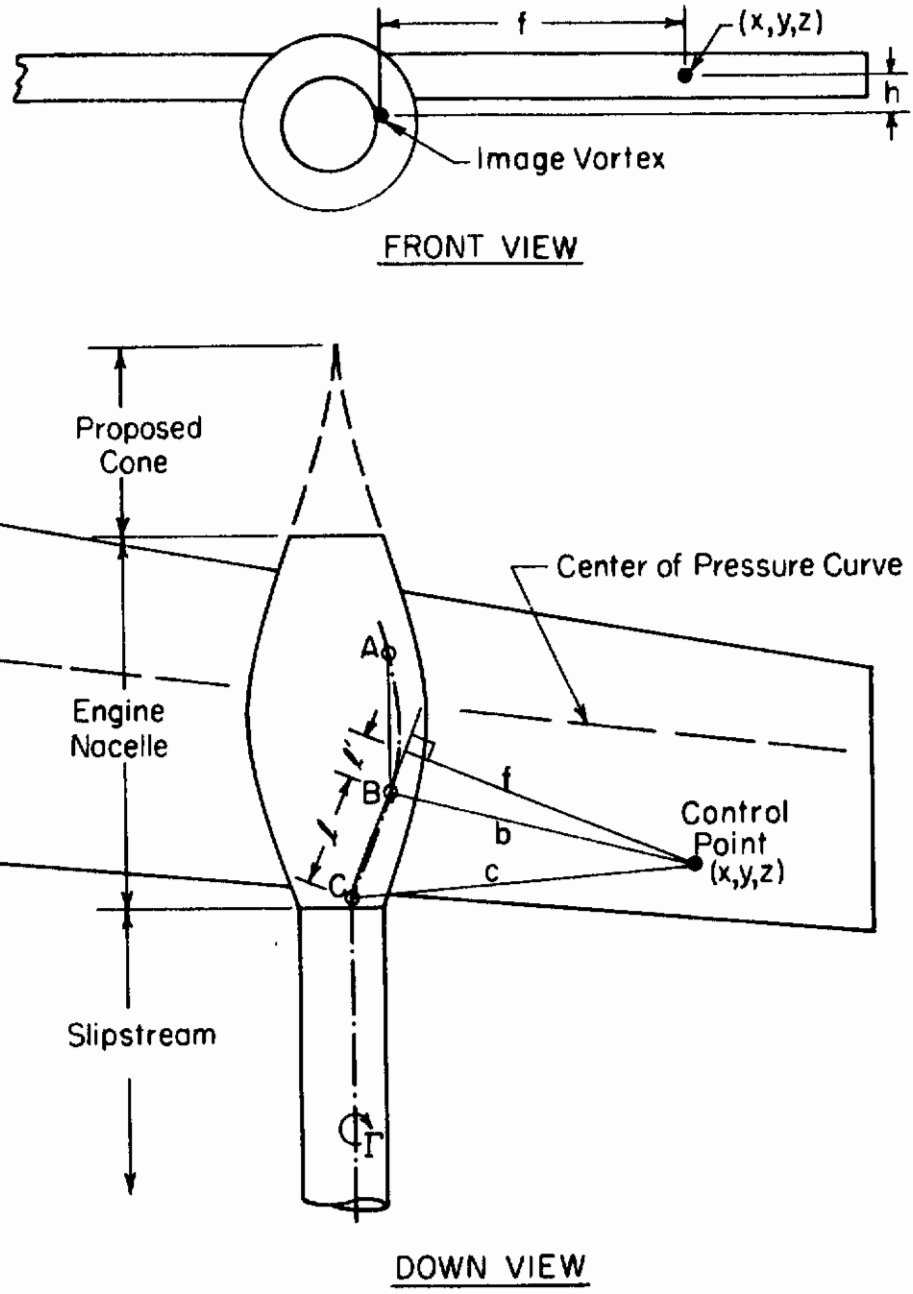

Figure 12. Image Vortex Inside a Nacelle

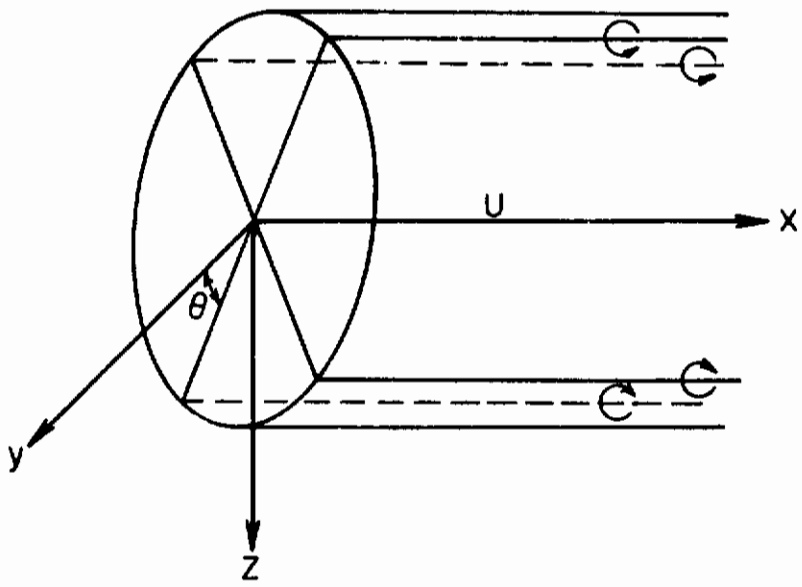

Figure 13. The Corresponding Vortex System of the Propeller Slipstream

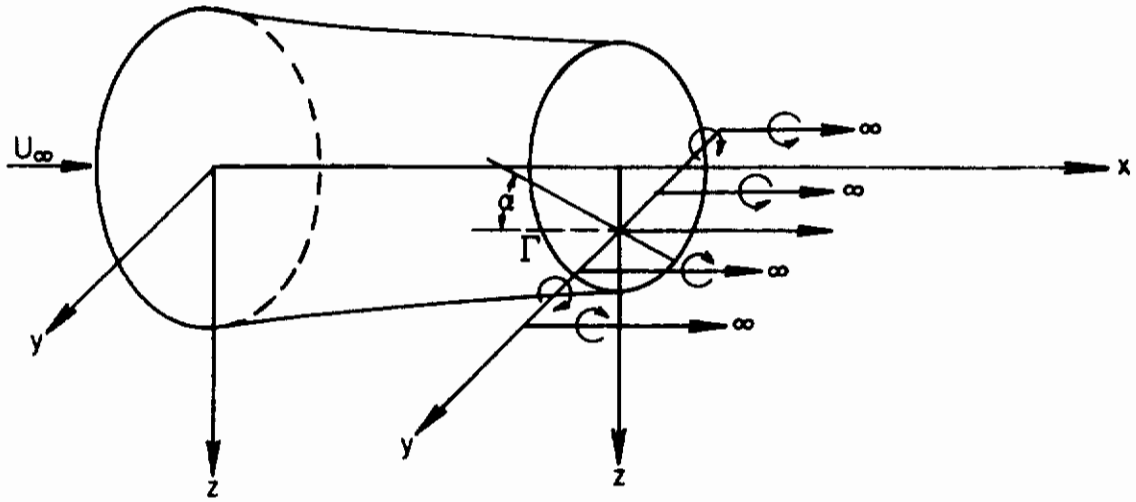

Figure 14. The Coordinate System and the Wing's Corresponding Vortex Sheet

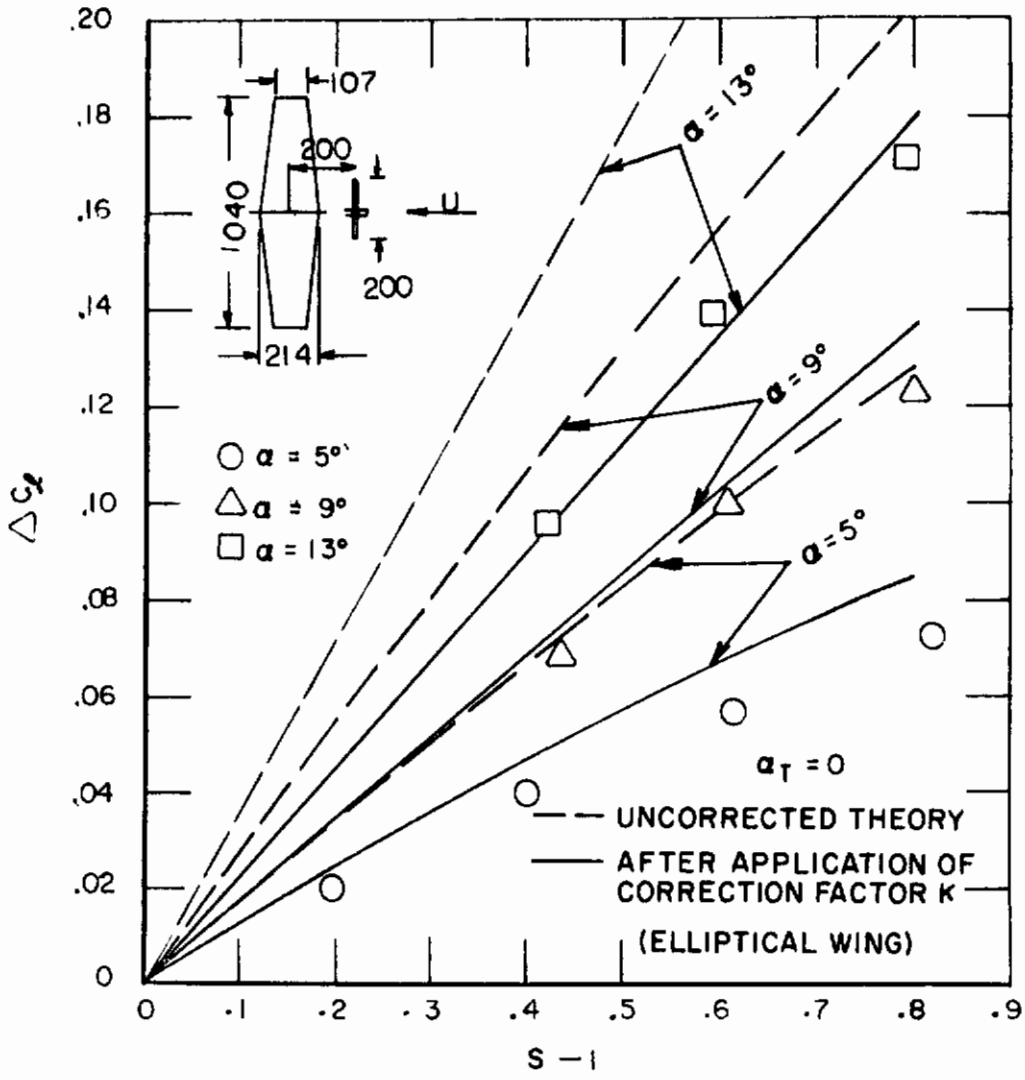

Figure 15. Experimental and Calculated Values of ΔC_ℓ (after Ferrari[4])

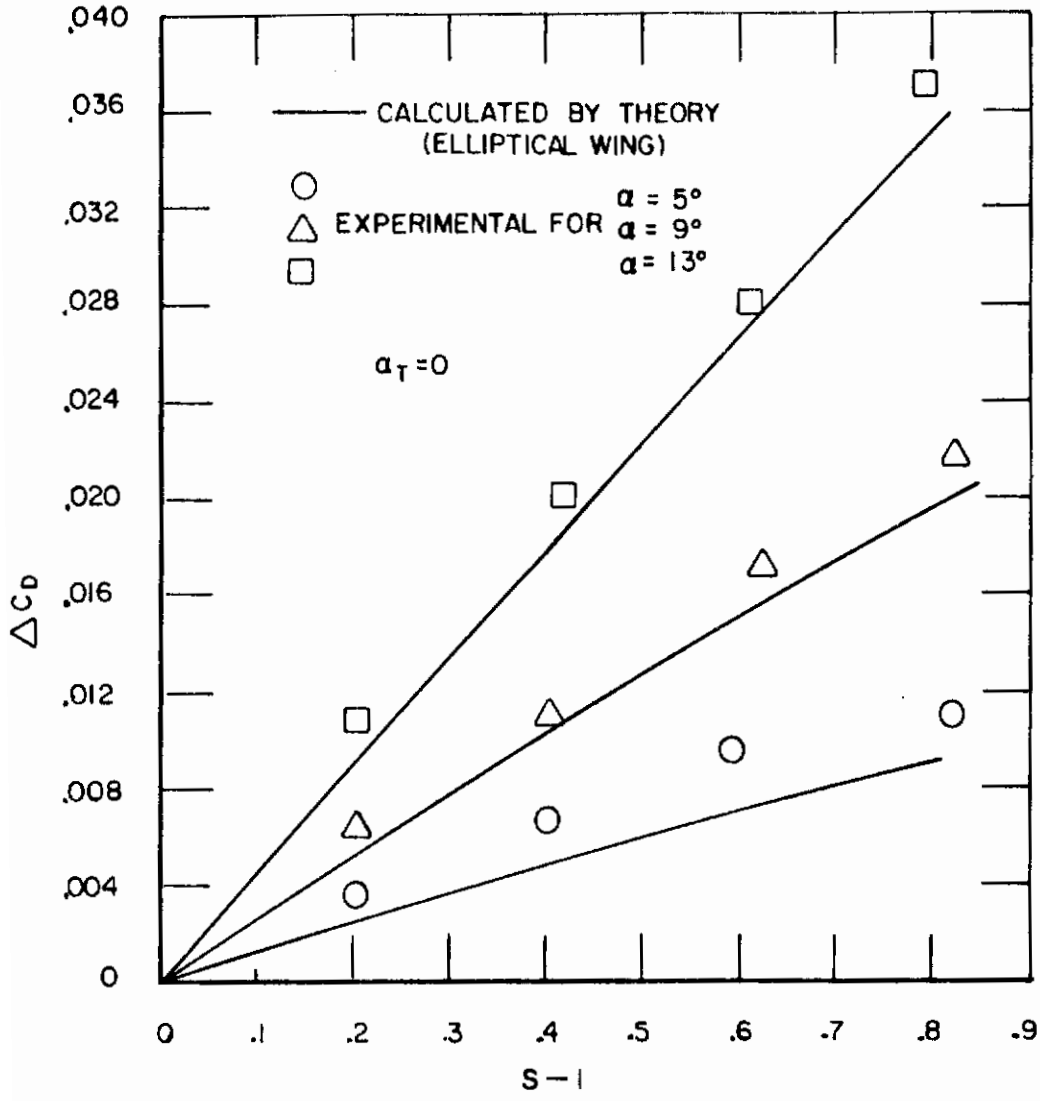

Figure 16. Experimental and Calculated Values of ΔC_D (after Ferrari[4])

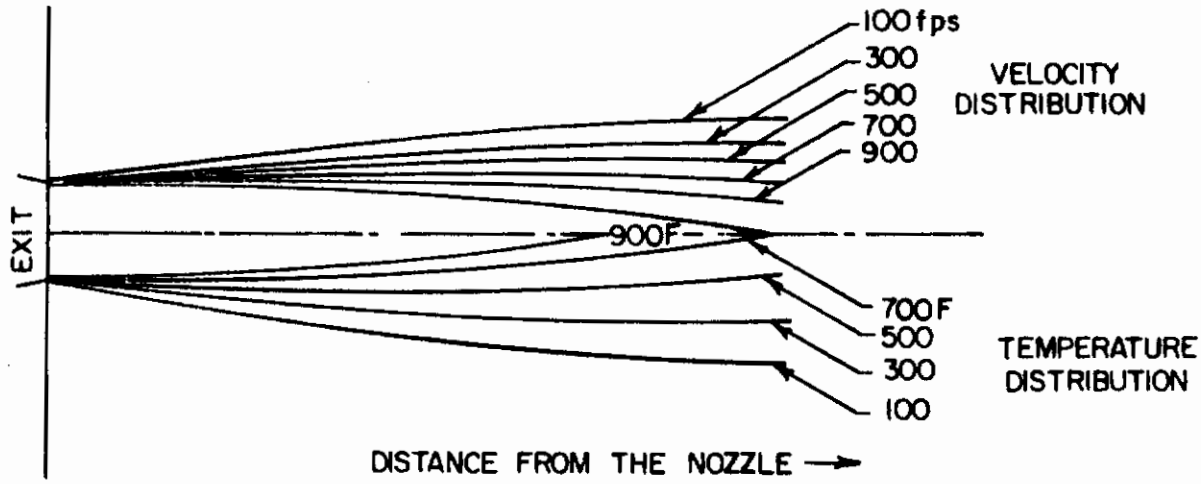

Figure 17. Jet Wake with Turbulent Mixing Profile for a Typical Jet Engine (Static Sea Level Case)